© 2022. Published by The Company of Biologists Ltd | Development (2022) 149, dev200450. doi:10.1242/dev.200450

STEM CELLS AND REGENERATION

RESEARCH ARTICLE

Dhx38 is required for the maintenance and differentiation of erythro-myeloid progenitors and hematopoietic stem cells by alternative splicing

Jiayi Tu[1,*], Shanshan Yu[2,*], Jingzhen Li[1], Mengmeng Ren[1], Yangjun Zhang[3], Jiong Luo[1], Kui Sun[1], Yuexia Lv[1], Yunqiao Han[1], Yuwen Huang[1], Xiang Ren[1], Tao Jiang[1], Zhaohui Tang[1], Mark Thomas Shaw Williams[4], Qunwei Lu[1,‡] and Mugen Liu[1,‡]

ABSTRACT

Mutations that occur in RNA-splicing machinery may contribute to hematopoiesis-related diseases. How splicing factor mutations perturb hematopoiesis, especially in the differentiation of erythro-myeloid progenitors (EMPs), remains elusive. Dhx38 is a pre-mRNA splicing-related DEAH box RNA helicase, for which the physiological functions and splicing mechanisms during hematopoiesis currently remain unclear. Here, we report that Dhx38 exerts a broad effect on definitive EMPs as well as the differentiation and maintenance of hematopoietic stem and progenitor cells (HSPCs). In *dhx38* knockout zebrafish, EMPs and HSPCs were found to be arrested in mitotic prometaphase, accompanied by a 'grape' karyotype, owing to the defects in chromosome alignment. Abnormal alternatively spliced genes related to chromosome segregation, the microtubule cytoskeleton, cell cycle kinases and DNA damage were present in the *dhx38* mutants. Subsequently, EMPs and HSPCs in *dhx38* mutants underwent P53-dependent apoptosis. This study provides novel insights into alternative splicing regulated by Dhx38, a process that plays a crucial role in the proliferation and differentiation of fetal EMPs and HSPCs.

KEY WORDS: Splicing factor, *dhx38*, Erythro-myeloid progenitors, Hematopoietic stem and progenitor cells, Cell cycle, DNA damage

INTRODUCTION

Alternative splicing is a fundamental regulatory mechanism of gene expression in higher organisms, requiring accurate regulation of RNA-splicing machinery (Baralle and Giudice, 2017). Mutations in components of the RNA-splicing machinery are present in >50% of myelodysplastic syndrome (MDS) patients, and nearly 60% of genes were predicted to undergo alternative splicing during human hematopoiesis (Chen et al., 2014). Emerging data show that splicing-factor mutations, to some degree, define distinct clinical phenotypes and often have different prognostic impacts (Pellagatti and Boultwood, 2020). Understanding the diversity and complexity of alternative splicing in hematopoiesis remains a challenge.

Hematopoiesis is a hierarchical system, in which hematopoietic stem and progenitor cells (HSPCs) differentiate into progressively committed progenitors and mature cells (Zhang et al., 2018). HSPCs maintain self-renewal and multilineage blood differentiation with a sophisticated mechanism to provide lifelong hematopoiesis. Dysplasia of HSPCs is frequently associated with an increased risk of hematopoiesis-related diseases, such as MDS and acute myeloid leukemia (Baeten and de Jong, 2018). Before the emergence of HSPCs, lineage-restricted progenitors, such as erythro-myeloid progenitors (EMPs), appear and overlap with the latter half of primitive hematopoiesis and the emergence of HSPCs from the dorsal aorta at 36 to 48 h post fertilization (hpf) (Da'as et al., 2012). EMPs give rise to fetal erythrocytes, myeloid lineages, natural killer cells and adult tissue-resident macrophages, and can be distinguished via the expression of *lmo2* and *gata1* (Dege et al., 2020; Li et al., 2018b; Bertrand et al., 2007, 2008; Forrester et al., 2012; Xia et al., 2021). Compromised EMPs impair the formation of fetal erythrocytes and adult macrophages, resulting in fetal hemoglobinopathy, late-onset neurodegeneration or chronic inflammatory diseases (Hoeffel et al., 2015; Mass et al., 2017; McGrath et al., 2011). Although several studies have been carried out to demonstrate the role of splicing factors in hematopoietic development, few studies have found the role of splicing factors in EMP defects.

EMPs and HSPCs both emerge from the hemogenic endothelium and differentiate into multiple blood cells. In this process, they share common and also distinct mechanisms of development (Yokomizo et al., 2018). For example, canonical Wnt signaling is a common mechanism regulating the emergence of EMPs and HSPCs (Frame et al., 2016). However, in a mechanism distinct from that of HSPCs, EMPs do not require Notch signaling during their appearance (Bertrand et al., 2010). HSPC dysfunction has been observed in splicing-factor knockout models, such as *sf3b1*, *ddx41* and *u2af1* (Danilova et al., 2010; De La Garza et al., 2016; Weinreb et al., 2021). However, the mechanism by which splicing factors regulate both the differentiation and maintenance of EMPs and HSPCs is still required to be fully determined.

dhx38 encodes the RNA helicase PRP16 and is required to destabilize the U2-U6 helix I between the first and second catalytic steps in the splicing pathway (Fica et al., 2017). Dhx38 is the only RNA helicase that binds to mitotic noncoding RNA, and interference with *DHX38* function in human cells affects mitotic function and leads to disrupted chromatin arrangement during the M phase (Nishimura et al., 2019). In fission yeast, mutations of Prp16

[1]Key Laboratory of Molecular Biophysics of Ministry of Education, College of Life Science and Technology, Huazhong University of Science and Technology, Wuhan 430074, P.R. China. [2]Institute of Visual Neuroscience and Stem Cell Engineering, College of Life Sciences and Health, Wuhan University of Science and Technology, Wuhan, Hubei 430065, P.R. China. [3]Tongji Hospital, Tongji Medical College, Huazhong University of Science and Technology, Wuhan 430030, P.R. China. [4]Charles Oakley Laboratories, Department of Biological and Biomedical Sciences, Glasgow Caledonian University, Glasgow G4 0BA, UK.
*These authors contributed equally to this work

‡Authors for correspondence (lium@mail.hust.edu.cn; luqw@hust.edu.cn)

J.T., 0000-0002-2626-0084; S.Y., 0000-0002-8748-5877; J.Luo, 0000-0002-1722-7565; Y.L., 0000-0003-1588-2547; Y.Huang, 0000-0003-0182-9972; Q.L., 0000-0003-4390-052X; M.L., 0000-0001-5076-8438

Handling Editor: Hanna Mikkola
Received 10 December 2021; Accepted 21 July 2022

Development (2022) 149, dev200450. doi:10.1242/dev.200450

affect a small subset of introns with weak 5′SS-U6 snRNA interactions (Vijayakumari et al., 2019). DHX38 is an endogenous inhibitor of the protein phosphatase PP4, which regulates DNA damage repair and microtubule development (Han et al., 2015). Missense mutations in *dhx38* affect the splicing of cell cycle-related genes and regulate heterochromatinization of the centromere. Latif et al. (2018) identified that the missense variant c.971G>A of *dhx38* is involved in the early-onset etiology of retinitis pigmentosa. However, there are no theoretical or experimental reports so far regarding the regulation of DHX38 in the hematopoietic system. We found that high expression of DHX38 was restricted to the lymphoid neoplasm diffuse large B-cell lymphoma and thymoma in the Gene Expression Profiling Interactive Analysis (GEPIA) database, and in 2006, DHX38 was reported to be amplified in acute myeloid leukemia (Ma et al., 2006). Whether and how DHX38 acts in the hematopoietic system needs to be further explored.

Zebrafish is an ideal model for investigating embryonic hematopoiesis, as it can survive for several days independently of the cardiovascular system (Li et al., 2018a). Here, we constructed a *dhx38* knockout zebrafish line, and observed its hematopoietic development during embryogenesis. Our study highlights the physiological function and splicing mechanisms of Dhx38 during hematopoiesis, and also demonstrates its role in regulating both EMPs and HSPCs.

RESULTS

dhx38 is highly expressed in the hematopoietic region

To establish the expression pattern of *dhx38* in zebrafish embryos, we performed whole-mount *in situ* hybridization (WISH) using a *dhx38* probe. We observed that *dhx38* was ubiquitously expressed throughout the zebrafish embryos. Outside of the head and tail, we also identified high expression of *dhx38* in the posterior blood island (PBI) at 36 hpf and in caudal hematopoietic tissue (CHT) at 48 hpf, where EMPs and HSPCs are known to colonize (Fig. S1A). Moreover, the *dhx38* promoter drove mCherry expression in the PBI at 36 hpf and colocalized with *cmyb* (or *myb*), a marker of EMPs and HSPCs (Bertrand et al., 2008; Hoeffel et al., 2015) (Fig. 1A,B). These data imply that the expression of *dhx38* is potentially required for the development of EMPs and HSPCs. We generated a *dhx38*$^{-/-}$ zebrafish line using CRISPR/Cas9 technology (Fig. 1C), with a

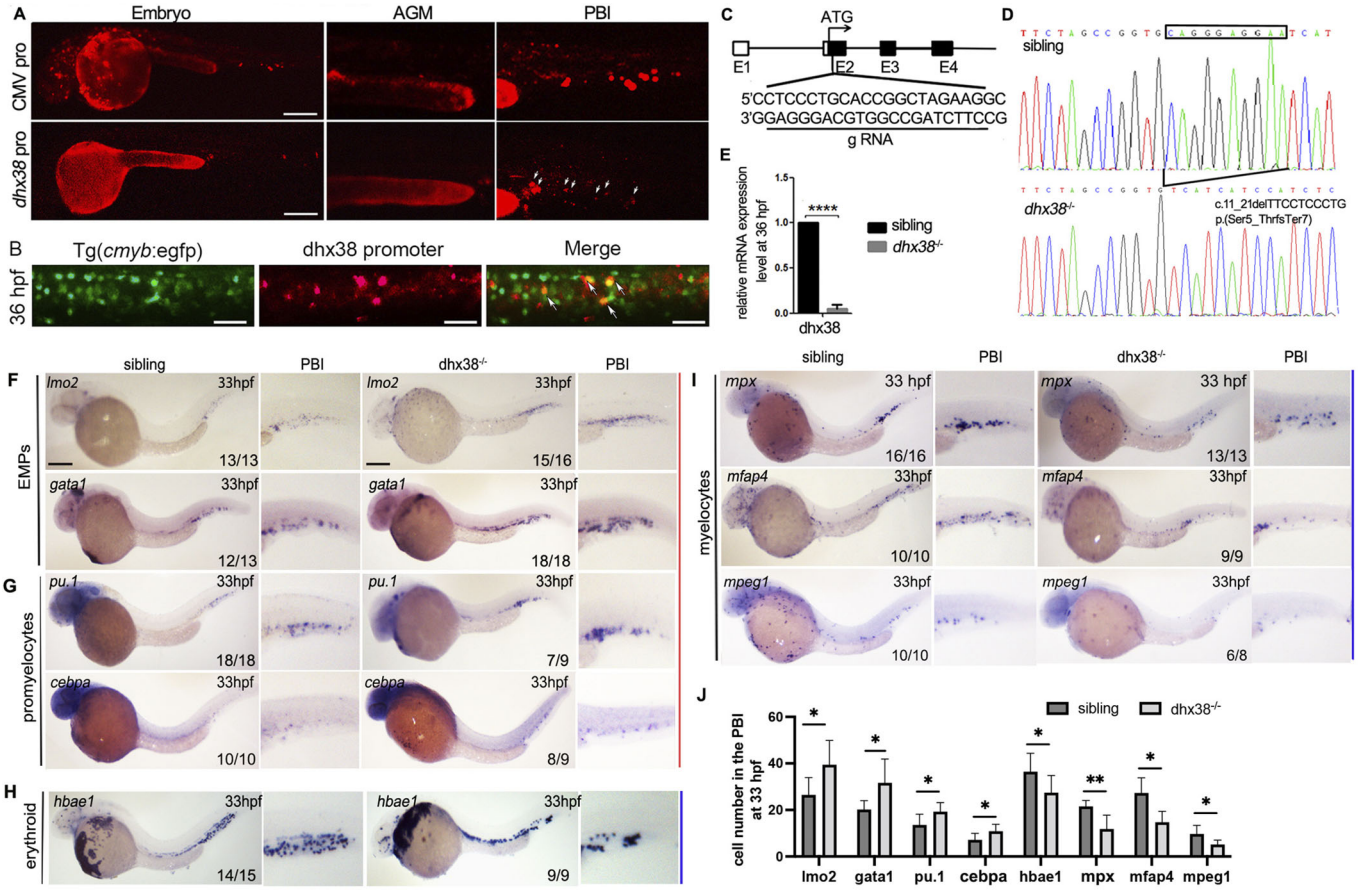

Fig. 1. Knockout of *dhx38* in zebrafish impaired EMP differentiation. (A) *In vivo* imaging of the expression of the CMV promoter vector and *dhx38* promoter vector in wild-type embryos. Scale bars: 200 µm. The *dhx38* promotor mainly drives mCherry expression in the PBI region (indicated by white arrows). (B) Representative images of *dhx38* expression in Tg(*cmyb*:eGFP) embryos at 36 hpf. White arrows indicate the co-expression of *dhx38* and *cmyb*. Scale bars: 50 µm. (C) A schematic diagram of the *dhx38* gRNA locus. (D) DNA sequencing identified a 10 bp deletion of cDNA (c.11_21delTTCCTCCCTG), which predicts a truncated protein (p.Ser5_ThrfsTer7). (E) qRT-PCR shows a significant decrease of *dhx38* mRNA in the *dhx38* mutants. (F,G) WISH results show that the expression of the EMP markers *lmo2* and *gata1* and the promyelocyte markers *pu.1* and *cebpa* in the *dhx38*$^{-/-}$ embryo is increased at 33 hpf. The red line denotes increased expression. Scale bars: 200 µm. (H,I) WISH results showing that the expression of the myelocyte markers *mpx*, *mfap4* and *mpeg1*, and the erythrocyte marker *hbae1* is decreased in the *dhx38* mutant at 33 hpf. The blue lines denote decreased expression. (J) Quantification of cell number in the PBI shown in F-I. Data show the mean±s.d. Significance was determined using a two-tailed, unpaired Student's *t*-test. **P*<0.05, ***P*<0.01; *****P*<0.0001.

Development (2022) 149, dev200450. doi:10.1242/dev.200450

10 bp deletion in *dhx38* cDNA (c.11_21delTTCCTCCCTG), which was predicted to generate a truncated protein (p.Ser5_ThrfsTer7) (Fig. 1D). The mRNA level of *dhx38* was undetectable in the *dhx38*$^{-/-}$ embryo at 36 hpf (Fig. 1E).

EMP differentiation is blocked in *dhx38*$^{-/-}$ zebrafish

Primitive hematopoiesis occurs as an early but transitory wave, generating primitive erythrocytes and macrophages at 12-26 hpf. The myeloid progenitor marker *pu.1* (also known as *spi1b*), erythroid progenitor marker *gata1* and hemangioblast marker *scl* (or *tal1*) are typically expressed in the lateral plate mesoderm of *dhx38* mutants at 13 hpf (Fig. S1B). The expression of myelocyte markers *mpx* and *lyz* in the rostral blood island and the erythrocyte marker *hbae1* (or *hbae1.1*) in the intermediate cell mass showed no difference between wild-type siblings and *dhx38* mutants at 24 hpf (Fig. S1C). Primitive hematopoiesis was unaffected in *dhx38*$^{-/-}$ zebrafish.

HSPCs originate from the arterial endothelium. The arterial marker *dll4* and venous marker *dab2* at 36 hpf showed no significant difference between *dhx38*$^{-/-}$ embryos and their wild-type siblings (Fig. S1D). In addition, the patterns of the dorsal aorta, posterior cardinal vein, caudal artery, caudal venous plexus and intersegmental vessels indicated well-developed angiogenesis in *dhx38*$^{-/-}$;Tg (*flk1*:mCherry) embryos at 36 hpf and 48 hpf (Fig. S1E). These data suggest that the development of the vasculature appears to be unaffected in the *dhx38* mutants.

Definitive hematopoiesis initiates through committed EMPs in the PBI that arise independently from HSPCs at 30-36 hpf (Bertrand et al., 2007). EMPs can differentiate into multiple lineages of blood cells, including erythrocytes, macrophages, granulocytes and mast cells, and are labeled by *gata1*$^{+}$/*lmo2*$^{+}$ double-positive cells (Bertrand et al., 2010). The expression of *lmo2*$^{+}$ and *gata1*$^{+}$ cells (EMPs) was normal at 30 hpf (Fig. S2A), but dramatically increased at 33 hpf in the PBI of *dhx38* mutants (Fig. 1F,J). We further examined the expression of genes downstream of EMP differentiation, including the promyelocyte markers *pu.1* and *cebpa*, which are highly expressed in immature cells and within undifferentiated myeloid cells in some hematopoietic cancers (Dai et al., 2016). Both cell types are expressed normally in the PBI of the *dhx38* mutant at 30 hpf (Fig. S2B), with expression increasing at 33 hpf (Fig. 1G,J), suggesting a crucial role of Dhx38 in mediating EMP development.

We investigated the expression of the mature granulocyte marker *mpx*, the mature macrophage marker *mfap4* (or *mfap4.1*), the macrophage marker *mpeg1* (or *mpeg1.1*) and the mature erythrocyte marker *hbae1* in the *dhx38* mutants and their wild-type siblings. The mRNA profiles were almost identical in their PBIs at 30 hpf (Fig. S2C), but decreased at 33 hpf and 36 hpf in the mutants (Fig. 1H-J; Fig. S3B). These results were confirmed by quantitative real-time PCR (qRT-PCR) (Fig. S3C).

Bertrand et al. isolated EMPs using *lmo2*$^{+}$/*gata1*$^{+}$ zebrafish at 30 hpf, and validated the tracing of EMP cells by using *cmyb*$^{+}$ and *gata1*$^{+}$ cells (Bertrand et al., 2010; Forrester et al., 2012). Consistent with our WISH results, the number of *gata1*$^{+}$/*cmyb*$^{+}$ cells and *pu.1*$^{+}$ cells in the PBI region of *dhx38* mutants was significantly increased compared with wild-type siblings at 36 hpf and 48 hpf, suggesting the accumulation of immature EMPs and promyelocytes in the *dhx38* mutants (Fig. 2A,B,G,H; Fig. S3A).

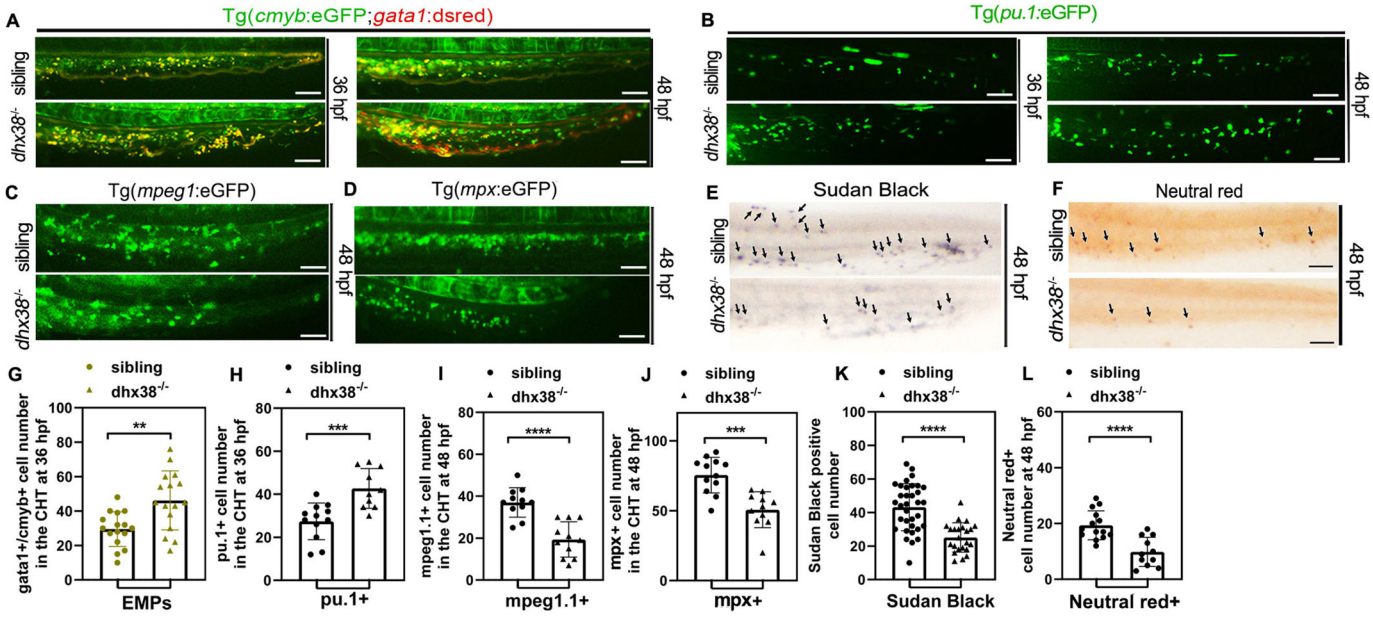

Fig. 2. Maturation of EMPs is perturbed in *dhx38* mutants. (A) *In vivo* imaging of *gata1*$^{+}$/*cmyb*$^{+}$ cells (EMPs) in the PBI region of Tg(*cmyb*:eGFP;*gata1*:dsred) fish. At 36 hpf and 48 hpf, the numbers of EMPs (indicated in yellow) in the *dhx38*$^{-/-}$ zebrafish are higher compared with wild-type siblings. Sibling, *n*=16; *dhx38*$^{-/-}$, *n*=16; performed with three replicates; ***P*=0.002. (B) *In vivo* imaging of Tg(*pu.1*:eGFP) fish shows that promyelocytes are increased in the PBI region of *dhx38* mutants at 36 hpf and 48 hpf. Sibling, *n*=12; *dhx38*$^{-/-}$, *n*=10; performed with three replicates; ****P*=0.0006. (C) *In vivo* imaging of macrophages in Tg(*mpeg1*:eGFP) also shows a decreased branched cell number in the *dhx38* mutant at 48 hpf. Sibling, *n*=11; *dhx38*$^{-/-}$, *n*=11; performed with three replicates; *****P*=0.00003. (D) *In vivo* imaging of granulocytes in Tg(*mpx*:eGFP) displays a decreased number in the *dhx38* mutant at 48 hpf. Sibling, *n*=12; *dhx38*$^{-/-}$, *n*=11; performed with three replicates; ****P*=0.00013. (E) Sudan Black staining in *dhx38*$^{-/-}$ zebrafish shows that mature granulocytes are decreased at 48 hpf. Black arrows indicate granulocytes. Sibling, *n*=34; *dhx38*$^{-/-}$, *n*=23; performed with three replicates; *****P*=0.000001. (F) Neutral Red staining shows significantly decreased numbers of functional macrophages. Black arrows indicate macrophages. Sibling, *n*=14; *dhx38*$^{-/-}$, *n*=11; performed with three replicates; ****P*=0.00014. (G-L) Quantification of cells from A-G. Significance was determined using a two-tailed, unpaired Student's *t*-test. ***P*<0.01; ****P*<0.001; *****P*<0.0001. All scale bars: 50 µm.

Development (2022) 149, dev200450. doi:10.1242/dev.200450

We then employed a zebrafish line, Tg(*mpeg1*$^{+}$:eGFP), to trace developing macrophages. Mature *mpeg1*$^{+}$ cells displayed a typical branched morphology in the PBI of wild-type siblings, but fewer branched mature macrophages in the PBI of *dhx38* mutants at 48 hpf (Fig. 2C,I). Granulocytes identified by Tg(*mpx*:eGFP) were also significantly reduced in the mutants (Fig. 2D,J). Taken together, these results suggest that EMP maturation is impaired in the *dhx38*$^{-/-}$ embryo. Embryos stained by Sudan Black showed a lower number of and smaller granulocytes, representing immature granulocytes, in *dhx38*$^{-/-}$ embryos than in wild-type siblings (Fig. 2E,K). Staining of phagocytic macrophages with Neutral Red showed that the number of functional macrophages in the PBI of *dhx38* mutant was significantly reduced (Fig. 2F,L). The increase in the number of immature blood cells and the reduction in the number of mature blood cells clearly show that EMP differentiation is blocked in the *dhx38*$^{-/-}$ embryo.

Loss of *dhx38* impairs definitive HSPC development

Similar to mammals, definitive hematopoiesis in zebrafish is divided into two independent stages: EMP development and HSPC development. WISH and fluorescent microscopy were employed to investigate whether loss of *dhx38* affects the development of definitive HSPCs in embryos. HSPCs labeled with a *cmyb* probe were correctly identified and localized in the ventral wall of dorsal aorta (VDA) of *dhx38* mutants at 36 hpf. Moreover, HSPCs in the *dhx38* mutants were found to be higher in number compared with their wild-type counterparts at 48 hpf, but this increase disappeared completely by 56 hpf (Fig. S3D). Fluorescence microscopy of *dhx38*$^{-/-}$;Tg(*flk*:mCherry;*cmyb*:eGFP) fish revealed that the formation of the hematogenic endothelium (*flk*$^{+}$;*cmyb*$^{+}$) in the VDA in *dhx38* mutants was comparable with that in the wild-type siblings at 36 hpf. HSPCs accumulated in the CHT at 48 hpf, but then subsequently decreased by 56 hpf in the CHT (Fig. 3A).

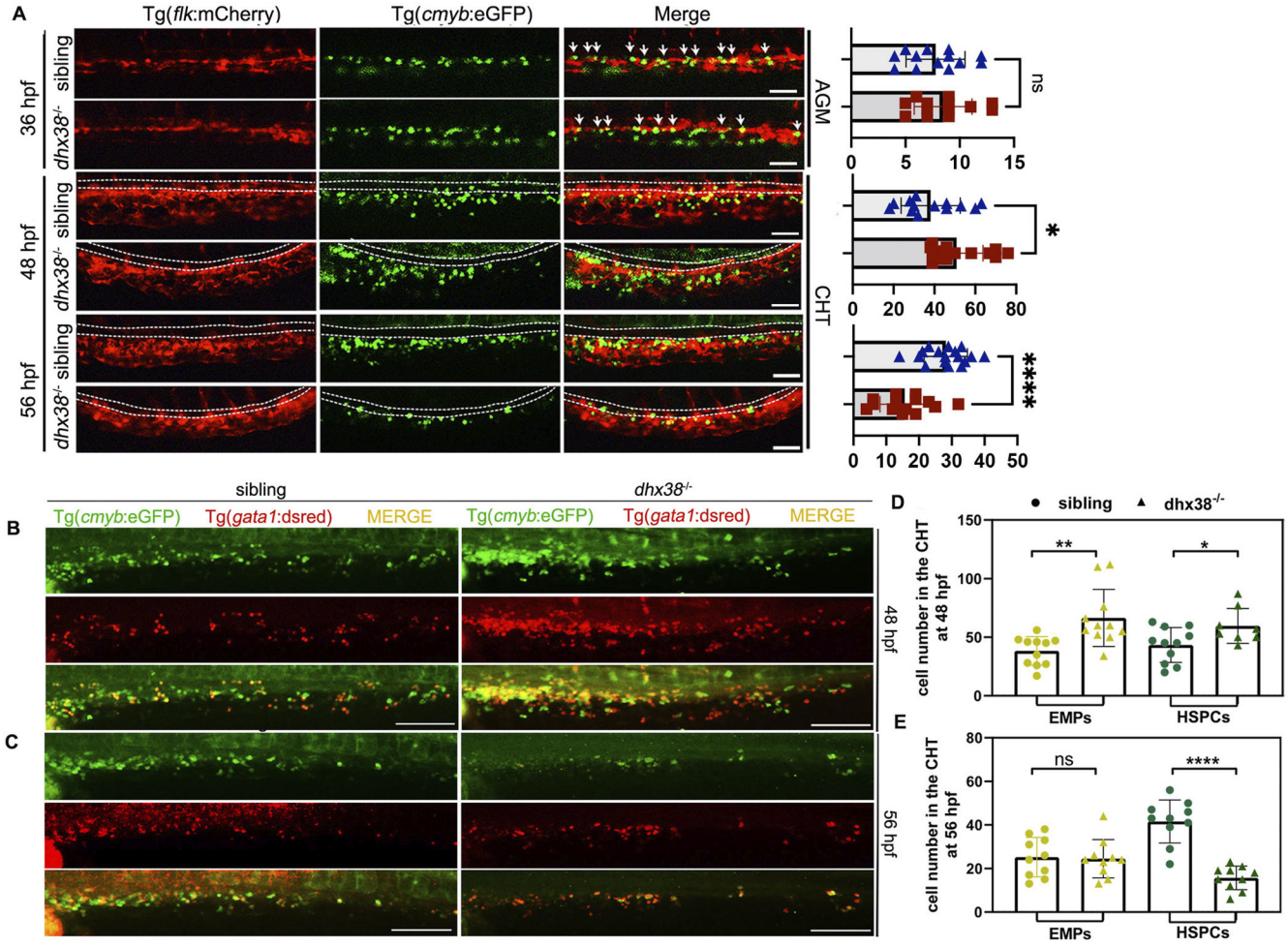

Fig. 3. Loss of *dhx38* impairs definitive hematopoiesis. (A) *In vivo* imaging of hematopoietic progenitor cells in Tg(*cmyb*:eGFP;*flk*:mCherry) at 36 hpf, 48 hpf and 56 hpf. The double-positive fluorescence (white arrows) in the VDA region shows that hemogenic endothelium emerges normally in the *dhx38* mutants. However, the number of *cmyb*$^{+}$ cells in the *dhx38* mutants are increased at 48 hpf, but decreased at 56 hpf. White dotted lines represent the caudal artery. For 36 hpf: sibling, *n*=13; *dhx38*$^{-/-}$, *n*=13; *P*=0.51, not significant. For 48 hpf: sibling, *n*=14; *dhx38*$^{-/-}$, *n*=19; **P*=0.016. For 56 hpf: sibling, *n*=19; *dhx38*$^{-/-}$, *n*=15; *****P*=0.000023. Quantification of cells from 36 hpf, 48 hpf, and 56 hpf is shown on the right. (B) Immunostaining of Tg(*cmyb*:eGFP;*gata1*:dsred) fish at 48 hpf shows an increase in the number of *cmyb*$^{+}$/*gata1*$^{+}$ cells (EMPs) and *cmyb*$^{+}$/*gata1*$^{-}$ cells (HSPCs) in the CHT of *dhx38* mutants. (C) Immunostaining of Tg(*cmyb*:eGFP;*gata1*:dsred) fish at 56 hpf demonstrates a decreased number of *cmyb*$^{+}$/*gata1*$^{+}$ EMPs and *cmyb*$^{+}$/*gata1*$^{-}$ HSPCs in the CHT of *dhx38* mutants. (D) Quantification of *cmyb*$^{+}$/*gata1*$^{+}$ and *cmyb*$^{+}$/*gata1*$^{-}$ cell numbers from B. Sibling, *n*=11; *dhx38*$^{-/-}$, *n*=11; EMPs, ***P*=0.0026; HSPCs, **P*=0.031. (E) Quantification of *cmyb*$^{+}$/*gata1*$^{+}$ and *cmyb*$^{+}$/*gata1*$^{-}$ cell number from C. Sibling, *n*=10; *dhx38*$^{-/-}$, *n*=10; EMPs, *P*=0.86; HSPCs, *****P*=0.0000009. Data show the mean±s.d. Significance was determined using a two-tailed, unpaired Student's *t*-test. n.s., not significant; **P*<0.05; ***P*<0.01; *****P*<0.0001. All scale bars: 200 µm.

Development (2022) 149, dev200450. doi:10.1242/dev.200450

The emergence of HSPCs was normal, whereas HSPC maintenance was perturbed in the *dhx38* mutants.

Given the impaired maintenance of HSPCs in *dhx38* mutants at 56 hpf, we examined the differentiation of HSPCs. Unsurprisingly, *dhx38*$^{-/-}$ embryos lacked the expression of the myeloid marker *lyz* and the erythroid marker *hbae1* in the CHT at 3 dpf, and the lymphoid mark *rag1* in the thymus at 4 dpf (Fig. S3E). Defects in HSPC maintenance in the *dhx38* mutants further resulted in a complete loss of lifelong hematopoiesis.

EMPs appear to overlap with the HSPCs in the PBI region from 30 hpf to 40 hpf, but can be distinguished by visualizing *cd41*$^{+}$/*gata1*$^{+}$ cells (EMPs) and *cd41*$^{+}$/*gata1*$^{-}$ cells (HSPCs), as previously reported (Bertrand et al., 2010, 2008; Forrester et al., 2012; Xia et al., 2021). We then distinguished HSPCs from EMPs by visualizing the *cmyb* and *gata1* markers in the PBI region. The numbers of both *cmyb*$^{+}$/*gata1*$^{+}$ and *cmyb*$^{+}$/*gata1*$^{-}$ cells were increased at 48 hpf, but decreased rapidly at 56 hpf in the *dhx38*$^{-/-}$ embryos (Fig. 3B-E), indicating that EMPs and HSPCs share similar dynamic characteristics, accumulating at first and then decreasing at later stages. Using an F0 strain, *dhx38* del7 (c.14_21delCTCCCTG), we also confirmed the role of *dhx38* in hematopoiesis, as this mutant phenocopied that of the *dhx38* del10 mutant (Fig. S8).

dhx38 deficiency induces abnormal cell cycle and apoptosis of EMPs and HSPCs

To further interrogate the biological basis by which EMPs and HSPCs accumulate in the *dhx38* mutants, we examined their proliferation. Experiments with 5-ethynyl-2'-deoxyuridine (EdU) revealed that the number of cells undergoing S phase was significantly reduced in the PBI of *dhx38*$^{-/-}$ embryo at 36 hpf (Fig. 4A-D). In contrast, immunofluorescence of phosphorylated histone H3 (pH3) showed that both cell types were arrested in the M phase in the PBI of *dhx38* mutants at 36 hpf (Fig. 4E-H). Meanwhile, pH3^{+} cells exhibited an abnormal chromosome karyotype in *dhx38*$^{-/-}$ embryos (Fig. S4A). Small interfering RNA (siRNA)-mediated interference of DHX38 in K562 leukemia cells phenocopied the G2/M arrest observed in the *dhx38* mutants (Fig. 4I; Fig. S4B). We hypothesized that the cell cycles of EMPs and HSPCs were arrested in the M phase in *dhx38*$^{-/-}$ embryos. Moreover, an enhanced DNA damage signal was observed in *dhx38* mutants at 36 hpf and 56 hpf, indicating an impaired cell cycle (Fig. 4J).

The numbers of EMPs and HSPCs were decreased in *dhx38*$^{-/-}$ embryos at 56 hpf. We therefore evaluated whether EMPs and HSPCs underwent apoptosis in *dhx38*$^{-/-}$ embryos, via the terminal deoxynucleotidyl transferase dUTP nick end labeling (TUNEL) assay. Although there was no significant difference between *dhx38* mutants and wild-type siblings with regards to the proportion of apoptotic EMPs at 36 hpf in the PBI (Fig. S4C,D), apoptosis increased significantly in the PBI of *dhx38*$^{-/-}$ embryos at 56 hpf (Fig. 4K-N). Also, inhibiting P53 (encoded by *p53* or *tp53*) activity in *dhx38* mutants failed to rescue the phenotype of granulocyte (*mpx*) and erythrocyte (*hbae3*) reduction at 36 hpf (Fig. 8C; Fig. S4E). Therefore, we eliminated the possibility that the changes in granulocyte and erythrocyte numbers in *dhx38* mutants at 36 hpf were due to defects in the viability of differentiated cells. But our findings strongly suggest that the observed reduced numbers of EMPs and HSPCs at 56 hpf are the result of increased apoptosis.

We then performed a more detailed investigation of mitosis by monitoring the state of the chromosomes and the spindle during mitosis in *dhx38*$^{-/-}$ embryos. A wide range of EMPs and HSPCs exhibited karyotypic abnormalities in the PBI of *dhx38*$^{-/-}$ zebrafish at 36 hpf and 48 hpf (Fig. 5A,B). In metaphase, EMPs and HSPCs in wild-type siblings exhibited a typical chromosome alignment on the equatorial plane, with spindles attached to the centromeres, whereas EMPs and HSPCs in the *dhx38* mutants displayed an increase in the impaired alignment of chromosomes. Intriguingly, a previous study found a similar chromatin phenotype, called the 'grape' phenotype, when DHX38 was depleted from HeLa cells (Nishimura et al., 2019). In anaphase, the *dhx38* mutants exhibited an abnormal chromatin phenotype accompanied by progressively abnormal spindle morphology (Fig. 5C-F; Fig. S5).

Lack of *dhx38* results in abnormal alternative splicing in cell cycle-related genes

We profiled the transcriptomes of the PBI region of wild-type siblings and mutants by RNA sequencing (RNA-seq) at 36 hpf. This analysis revealed that 164 downregulated genes and 386 upregulated genes were mainly enriched in centromere-related genes and the P53 signaling pathway (Fig. S6A-C; Tables S1 and S2). These findings are consistent with the observation of abnormal mitosis and increased apoptosis in *dhx38* mutants. As Dhx38 mainly mediates the splicing process of pre-mRNA, we speculate that abnormal splicing events may be the cause of hematopoietic abnormalities. RNA-seq analysis revealed 150 genes with retained introns (RI), 685 genes with skipped exons (SE) and 131 alternatively spliced genes (i.e. genes containing an alternative 3′ splice site or A3SS, an alternative 5′ splice site or A5SS, or a mutually exclusive exon, MXE) were differentially expressed in *dhx38*$^{-/-}$ embryos (Fig. 6A; Table S3). The most significant events in differential splicing events are displayed in percent spliced in index (PSI) DOWN of SE events (600/966) and PSI UP of RI events (145/966), which implies an increase in exon skipping and intron retention (Fig. 6A). Compared with the unaffected splice sites, the PSI DOWN group of SE events have significantly longer 3′ and 5′ introns and shorter exons. Meanwhile, the PSI UP group of RI events showed shorter introns. The PSI DOWN group of SE events displayed that the exons have lower GC content (Fig. 6C). The shorter length of affected exons/introns and lower GC content may require higher accuracy for splicing factors, and therefore may be more sensitive to *dhx38* deletion.

The biological processes of the cell cycle, double-strand break repair, the microtubule cytoskeleton and chromosome segregation were mainly enriched among all the differentially spliced events (Fig. 6B,D). They were verified by semi-quantitative PCR (semi-qPCR) and qRT-PCR in wild-type sibling and *dhx38* mutants (Fig. 7A,B; Fig. S7). Significant splicing changes and decreased expression were observed in genes such as those involved in chromatin segregation (*mis18a*, *cenpk*, *kdm8*, *smc5* and *knl1*) and those related to cell cycle kinases (*ccng2*, *ccnb2* and *aaas*), DNA damage (*dtl*, *trip12*, *rad9a*, *eme1*, *tonsl* and *recql*) and the microtubule cytoskeleton [*scrib*, *ift20*, *cep131*, *lzts2a*, *sept6* (also known as *septin6*), *mak* and *pard3ab*]. Many of these genes are components of centrioles or the spindle apparatus. Previous studies have shown that *cenpk*, *mis18a* and *knl1* mediate centromeric functions (Cheeseman et al., 2008; Medina-Pritchard et al., 2020). The *smc5* and *kdm8* genes are involved in chromatin segregation during mitosis (Hsia et al., 2010; Wehrkamp-Richter et al., 2012). Loss of function of *ccng2* and *ccnb2* has been shown to result in a defect in chromatin condensation (Gong and Ferrell, 2010). *aaas* (also known as *aladin*) is a spatial regulator of Aurora A, which plays a critical role in multiple steps of mitotic progression (Carvalhal et al., 2015). The *scrib*, *ift20*, *cep131*, *lzts2a*, *sept6*, *mak*

Development (2022) 149, dev200450. doi:10.1242/dev.200450

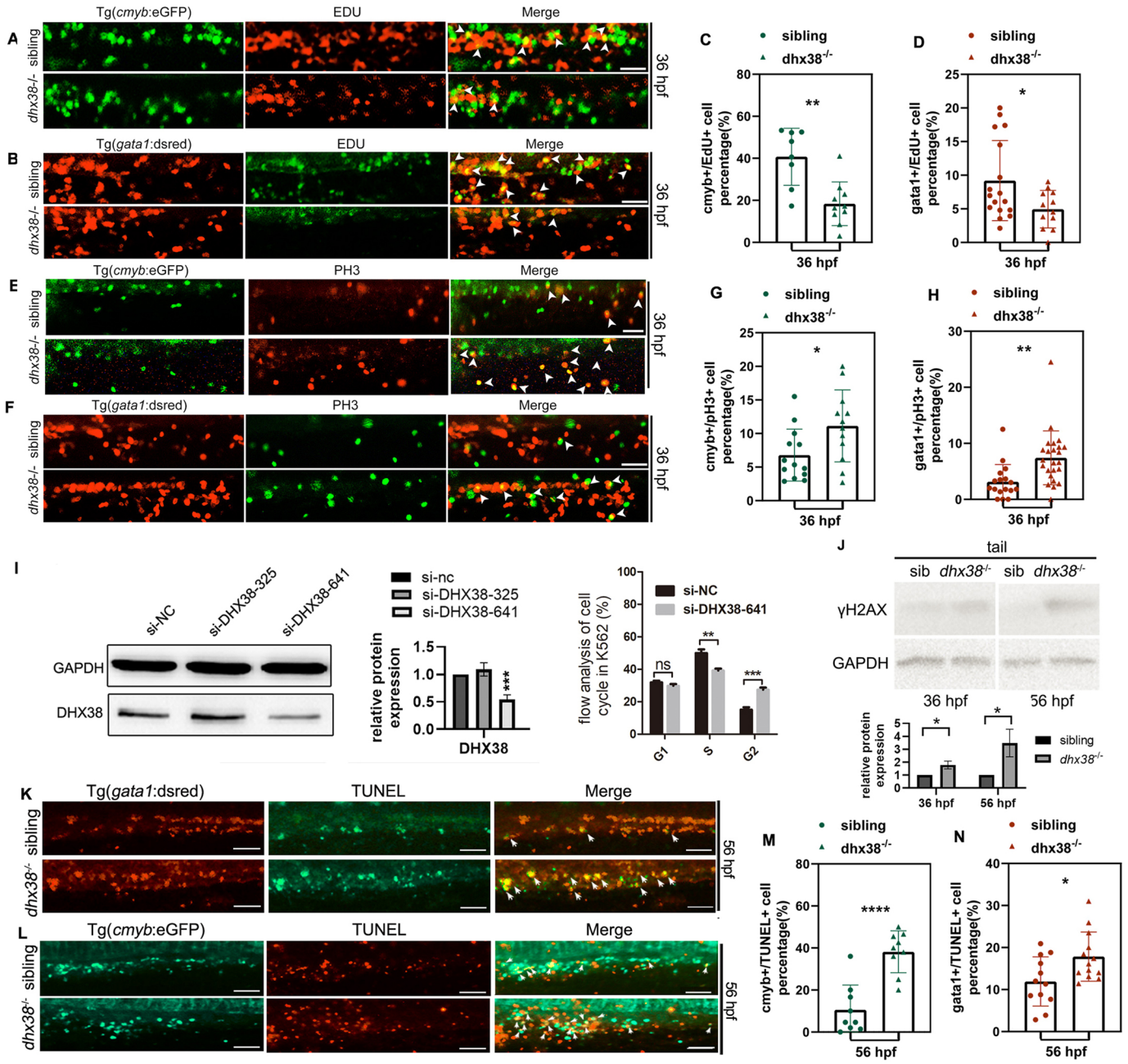

Fig. 4. Dhx38 deficiency induces abnormal mitosis and apoptosis of EMPs and HSPCs in zebrafish. (A) EdU assay in Tg(*cmyb*:eGFP) indicates an increase of *cmyb*$^{+}$ cells in the S phase of *dhx38*$^{-/-}$ embryos at 36 hpf. White arrows indicate the colocalization of *cmyb* and EdU. Sibling, *n*=8; *dhx38*$^{-/-}$, *n*=10; performed with three replicates; ***P*=0.001. (B) EdU assay in Tg(*gata1*:dsred) indicates an increase in the number of *gata1*$^{+}$ cells in the S phase in *dhx38*$^{-/-}$ embryos at 36 hpf. White arrowheads indicate the colocalization of *gata1* and EdU. Sibling, *n*=17; *dhx38*$^{-/-}$, *n*=12; performed with three replicates; **P*=0.029. (C,D) Quantification of *cmyb*$^{+}$ EdU^{+} cells and *gata*$^{+}$ EdU^{+} cells from A,B, respectively. (E) Double immunostaining of Tg(*cmyb*:eGFP) and pH3 shows that the number of *cmyb*$^{+}$ cells in the M phase is elevated in the *dhx38* mutants at 36 hpf. White arrowheads indicate the colocalization of *cmyb* and pH3. sibling, *n*=13; *dhx38*$^{-/-}$, *n*=12; performed with three replicates; **P*=0.028. (F) Double immunostaining of Tg(*gata1*:dsred) and pH3 shows that the number of *gata1*$^{+}$ cells in the M phase is also elevated in *dhx38* mutants at 36 hpf. White arrowheads indicate the colocalization of *gata1* and pH3. Sibling, *n*=17; *dhx38*$^{-/-}$, *n*=24; performed with three replicates; ***P*=0.0025. (G,H) Quantification of *cmyb*$^{+}$ pH3^{+} cells and *gata*$^{+}$ pH3^{+} cells from E,F, respectively. (I) The siDHX38-641 siRNA is at the c.641 position of the human DHX38 gene, and siDHX38-328 is at c.328. The silencing efficiency of these two siRNAs was confirmed by western blotting (left). Western blotting for DHX38 shows the efficiency of DHX38 knockdown by si-DHX38-641, but not by si-DHX38-325 (middle). Flow cytometry analysis of the cell cycle (right) after treatment with si-DHX38-641, showing a decrease of cells in the S phase and an increase of cells in the M phase. Performed with six replicates; n.s., *P*=0.18; ***P*=0.001; ****P*=0.0001. (J) The protein levels of γH2AX in siblings and *dhx38*$^{-/-}$ zebrafish at 36 and 56 hpf were detected by western blotting. GAPDH was used to normalize protein loading. *n*=3; for 36 hpf, **P*=0.01; for 48 hpf **P*=0.015. (K,L) TUNEL assay in Tg(*cmyb*:eGFP) (bottom) and Tg(*gata1*:dsred) (top) shows that apoptotic *cmyb*$^{+}$ and *gata1*$^{+}$ cells are increased in the *dhx38* mutants at 56 hpf. The double-positive fluorescence demonstrates that *cmyb*$^{+}$ and *gata1*$^{+}$ cells underwent apoptosis. For Tg(*gata1*:dsred): sibling, *n*=12; *dhx38*$^{-/-}$, *n*=13; performed with three replicates; **P*=0.019. For Tg(*cmyb*:eGFP): sibling, *n*=9; *dhx38*$^{-/-}$, *n*=9; performed with three replicates; *****P*=0.00006. (M,N) Quantification of double-positive fluorescent cell number from K,L. Data show the mean±s.d. Significance was determined using a two-tailed, unpaired Student's *t*-test. n.s., not significant; **P*<0.05; ***P*<0.01; ****P*<0.001; *****P*<0.0001. All scale bars: 50 µm.

Development (2022) 149, dev200450. doi:10.1242/dev.200450

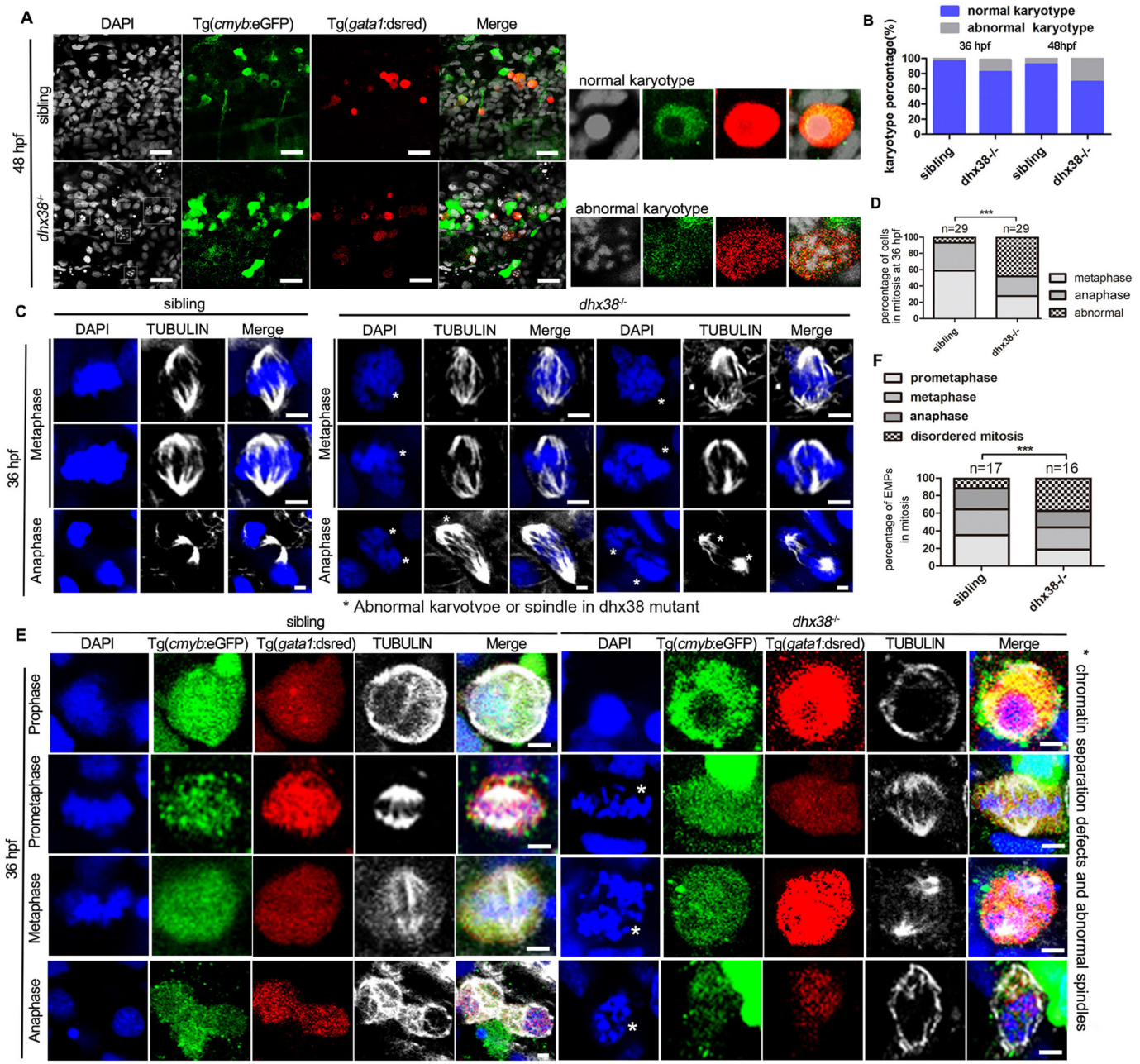

Fig. 5. EMPs in *dhx38* mutants exhibit disordered mitosis. (A) Confocal images of immunostaining of Tg(*cmyb*:eGFP;*gata1*:dsred) fish and DAPI (white) show that an abnormal karyotype occurs in the *dhx38* mutants at 48 hpf. The gray boxes indicate cells with abnormal karyotypes. (B) Quantification of cells with abnormal karyotypes. For 36 hpf, number of cells with abnormal karyotypes: sibling, 32/768; *dhx38*$^{-/-}$, 128/820. For 48 hpf, number of cells with abnormal karyotypes: sibling, 64/736; *dhx38*$^{-/-}$, 248/552. (C) Confocal images of immunostaining for α-tubulin and DAPI. The first three panels in the wild-type siblings show a normal karyotype and spindles during metaphase and anaphase. The last six panels in *dhx38*$^{-/-}$ show a 'grape' karyotype in metaphase. The 'grape' karyotype appears to represent chromosomes unable to align at the equatorial plate, and these cells progress to disordered anaphase in *dhx38*$^{-/-}$ embryos. Asterisks indicate abnormal karyotypes or spindles. (D) Quantification of double-positive fluorescent cell number from C. (E) Confocal images of immunostaining for *cmyb* (green), *gata1* (red), DAPI (blue) and α-tubulin (white) at 36 hpf. EMPs (*cmyb*$^{+}$/*gata1*$^{+}$) undergo normal prometaphase, metaphase and anaphase in siblings, but exhibit an abnormal chromatin karyotype accompanied by a progressively abnormal spindle morphology in the *dhx38* mutants. Asterisks represent abnormal mitotic processes. (F) Quantification of the percentage of EMPs in mitosis from E. Scale bars: 50 µm (A); 5 µm (C,E). ***P<0.001.

and *pard3ab* gene products participate in microtubule motor activity and microtubule polymerization (Carvalho et al., 2015; Chen et al., 2009; Holdgaard et al., 2019; Hong et al., 2010; Sudo and Maru, 2008; Wang and Kung, 2012; Zhu et al., 2017). The *dtl*, *trip12*, *rad9a*, *eme1*, *tonsl* and *recql* genes are essential for genome integrity and chromosomal stability (Calzetta et al., 2020; Gatti et al., 2020; Huang et al., 2019; Piwko et al., 2016; Sansam et al., 2006). Of the genes assessed, *cenpk*, *smc5*, *knl1*, *kdm8*, *eme1*, *tonsl*, *ccng2*, *ccnb2* and *aaas* are predicted to undergo premature termination codon-nonsense-mediated mRNA decay (PTC-NMD) events, whereas *trip12*, *scrib*, *pard3ab*, *sept6*, *ift20* and *lzts2a* undergo differential isoform transition, with *mis18a*, *dtl*, *rad9a*, *mak* and *cep131* generating disordered isoforms (Fig. 7C).

Development (2022) 149, dev200450. doi:10.1242/dev.200450

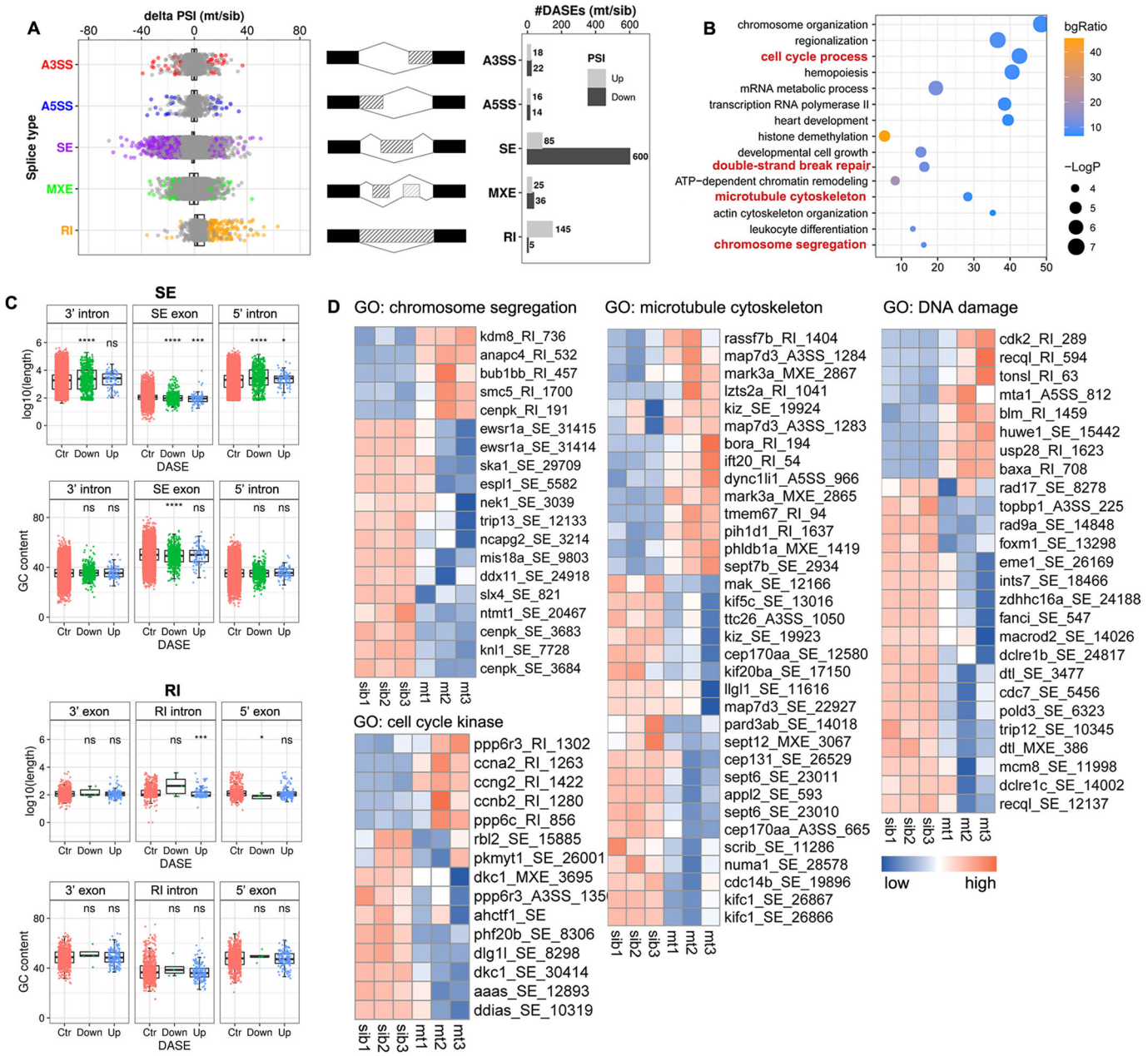

Fig. 6. Lack of *dhx38* results in abnormal alternative splicing in the cell cycle. (A) Categories of differentially spliced genes based on the changed PSI value in the *dhx38* mutants (mt). The percent spliced in index (PSI) indicates the efficiency of splicing a specific exon into the transcript population of a gene. Exons/intron that are constitutively retained in all transcripts and are never skipped have a PSI of 100. Thus, PSI UP indicates exons/introns that are more likely to be retained in the mutants and PSI DOWN indicates exons/introns that more frequently skipped in the mutants. Differential alternative splicing events, DASEs; alternative 3′ splice site, A3SS; alternative 5′ splice site, A5SS; skipped exon, SE; retained intron, RI; mutually exclusive exon, MXE. (B) Gene Ontology (GO) analysis of differentially spliced genes shows that they are significantly enriched in chromatin organization, microtubule cytoskeleton, cell cycle and DNA damage. (C) Sequence lengths and GC content around normal splicing sites and abnormal splicing sites in SE and RI events of *dhx38* mutants. In SE events, the length of PSI DOWN group of 3' and 5' introns is longer than the PSI control group, but the length of PSI UP group of introns in RI events is shorter. This suggests that longer introns in SE events and shorter introns in RI events are more likely to respond to the *dhx38* loss of function. The PSI DOWN group of GC content around the exon in differential SE events is lower in the *dhx38* mutants. This demonstrates that exons with lower GC content are more likely skipped when *dhx38* is knocked out. n.s., not significant; **P*<0.05; ****P*<0.001; *****P*<0.0001. (D) Heat maps of differentially spliced genes enriched in chromosome segregation, microtubule cytoskeleton, cell cycle kinase and DNA damage.

Given the essential role of these alternatively spliced genes in mitosis, these observations likely explain the abnormal mitosis events observed in the *dhx38* mutants. Western blotting of CCNB2 in si-DHX38-641-treated cells also displayed decreased protein expression, compared with that in cells treated with negative control siRNA (si-NC) or si-DHX38-325 (Fig. 7D). All the isoform transition or NMD events of differentially spliced genes are provided in Tables S3 and S4.

dhx38 mutants undergo P53-dependent apoptosis

Accumulation of EMPs and HSPCs was followed by induction of apoptosis. The expression of *p53* and its target genes *p21* (also

Development (2022) 149, dev200450. doi:10.1242/dev.200450

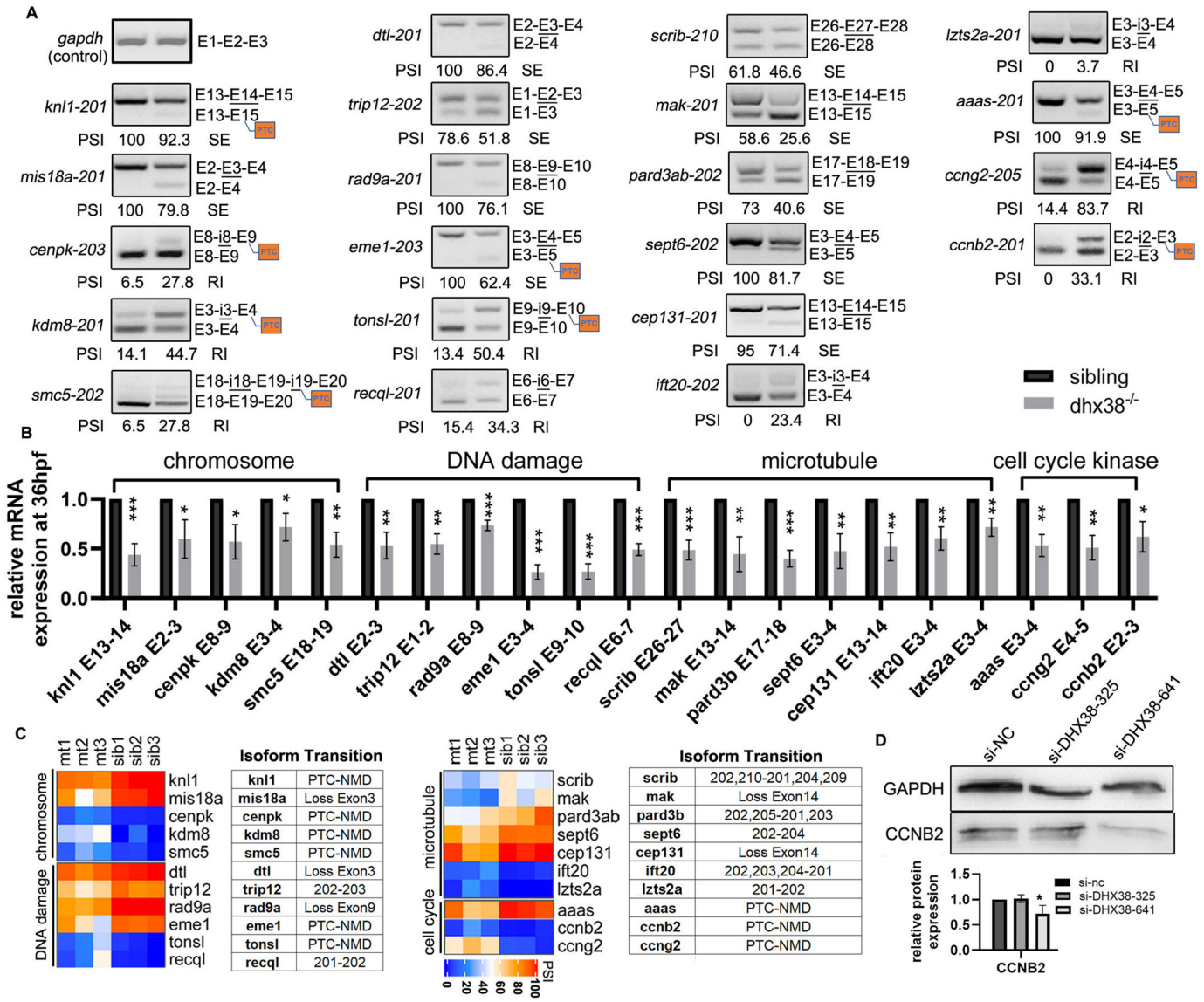

Fig. 7. *dhx38* modulates the alternative splicing of a subset of genes involved in mitosis and DNA damage. (A) Semi-qPCR confirms the abnormal splicing of the genes shown in Fig. 6D. The left band represents gene splicing in the wild-type siblings, whereas the right band represents splicing in the *dhx38* mutants. Percent spliced in, PSI; skipped exon, SE; retained intron, RI; exon, E; intron, I; premature termination codon, PTC. Black underlines denote abnormally spliced exons/introns. Experiments were performed with three replicates; *gapdh* was used as the internal control. (B) qRT-PCR analysis confirming mRNA expression of differentially spliced genes shown in Fig. 6D. $n \geq 12$ per group, performed with three replicates; *gapdh* was used as the internal control. Data show the mean±s.d. Significance was determined using two-tailed unpaired Student's *t*-test; **P*<0.05; ***P*<0.01; ****P*<0.001. (C) The genes shown here are those with splicing abnormalities and downregulated expression, which were by semi-qPCR and qRT-PCR, respectively. Of the genes assessed, *cenpk*, *smc5*, *knl1*, *kdm8*, *eme1*, *tonsl*, *ccng2*, *ccnb2* and *aaas* are predicted to undergo PTC-NMD events, whereas *trip12*, *scrib*, *pard3ab*, *sept6*, *ift20* and *lzts2a* undergo differential isoform transition, with *mis18a*, *dtl*, *rad9a*, *mak* and *cep131* generating disordered isoforms. (D) Western blotting for CCNB2 in the si-DHX38-641 displays decreased protein expression compared with the si-NC or si-DHX38-325 group. *n*=3, **P*=0.041.

known as *cdkn1a*), *mdm2* and *puma* (or *bbc3*) is upregulated in *dhx38*$^{-/-}$ embryos (Fig. 8A). The levels of the P53 protein also appeared to be overly increased in the mutants at 56 hpf (Fig. 8B). WISH assays revealed increased expression of *p53* in the CHT of the mutants at 36 hpf and in the aorta-gonad-mesonephros and CHT of the mutants at 56 hpf (Fig. 8C,G). We rescued the embryos by inhibiting P53 activity. As expected, the number of HSPCs at 56 hpf was significantly increased after incubation with 1 µM of the P53 inhibitor PFT-β in the *dhx38* mutants (Fig. 8D,E,H-J). Both treatment with PFT-β and *p53* knockout extended the survival ratio of the *dhx38* mutants (Fig. 8F). Taken together, these data suggest that the induction of apoptosis in *dhx38* mutant is P53 dependent.

DISCUSSION

In this study, our findings demonstrate that Dhx38 is essential for the maintenance and differentiation of EMPs and HSPCs during zebrafish embryogenesis. The importance of EMPs in fetal hematopoiesis has not been fully elucidated to date. Herein, we emphasize the key role of the splicing factor Dhx38 in EMP development. In *dhx38*$^{-/-}$ zebrafish, EMPs accumulated, but failed to differentiate into mature myeloid cells. This result suggests that loss of *dhx38* may lead to fetal hematopoiesis defects, which may prevent the embryo from surviving. Moreover, EMPs give rise to macrophage precursors that distribute within embryonic tissues and differentiate into adult tissue-resident macrophage subsets, such as

Development (2022) 149, dev200450. doi:10.1242/dev.200450

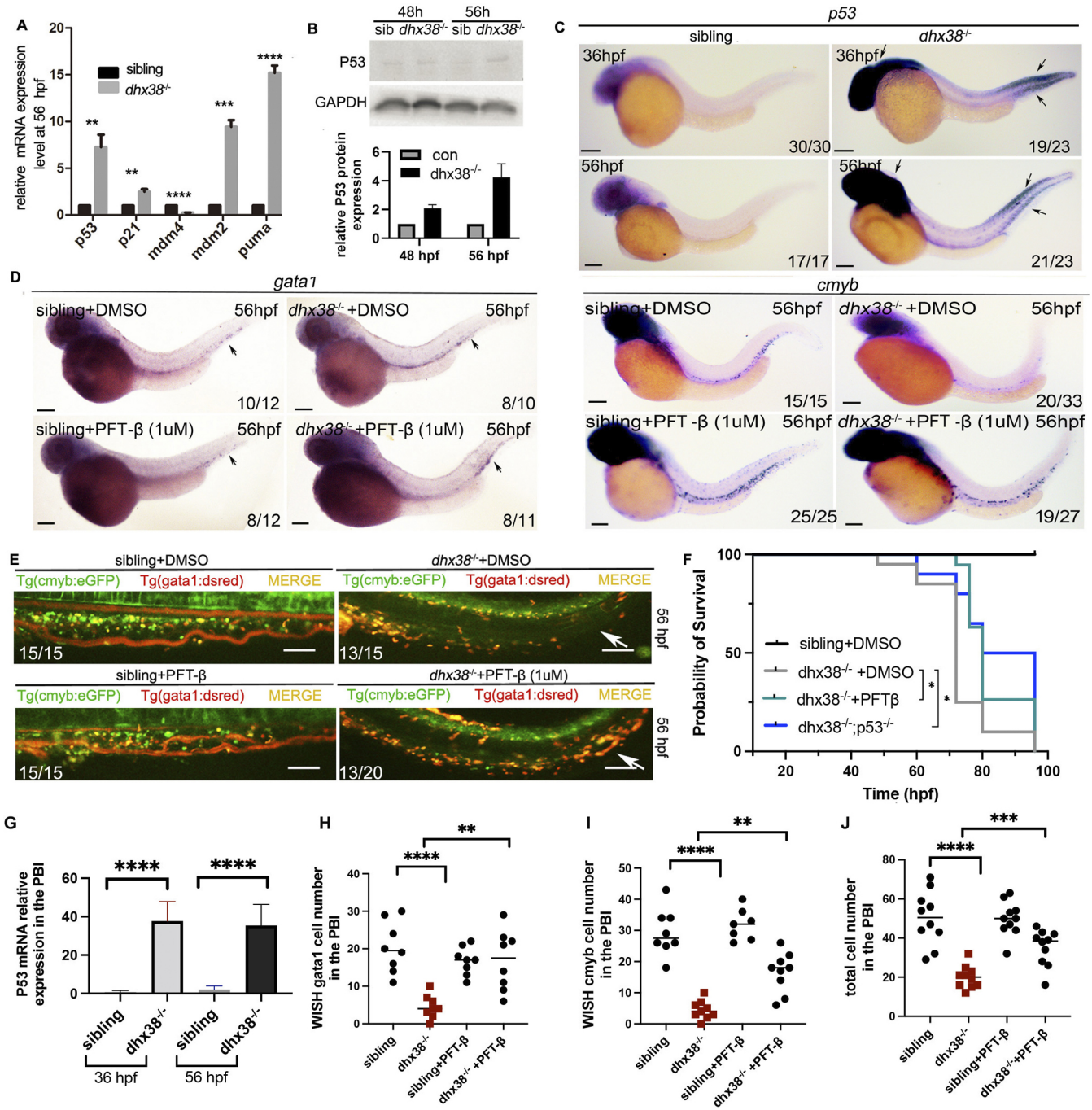

Fig. 8. EMPs and HSPCs in the *dhx38* mutants undergo P53-dependent apoptosis. (A) qRT-PCR analysis of the genes involved in P53 signaling shows a significant increase in the expression of *p53*, *p21*, *puma*, *mdm4* and *mdm2*. $n \geq 12$ per group. Experiments were performed with three replicates; *gapdh* was used as an internal control. (B) Western blotting analysis shows an increased expression of P53 in *dhx38*$^{-/-}$ zebrafish at 48 hpf, which increases further at 56 hpf. (C) The expression pattern of *p53* detected by WISH reveals that P53 begins to accumulate in the PBI at 36 hpf and 56 hpf. Black arrows indicate the expression of *p53*. (D) Decreased expression of *cmyb* (right) and *gata1* (left) in the *dhx38* mutants can be rescued following incubation with the P53 inhibitor PFT-β (1 µM). Black arrows indicate the expression of *gata1*. (E) *In vivo* imaging of hematopoietic progenitor cells in Tg(*cmyb*:eGFP;*gata1*:dsred) at 56 hpf. The overall number of hematopoietic progenitor cells in the PFT-β group was higher than in the DMSO group. White arrows indicate blood cells in the CHT region. (F) The survival curve shows that PFT-β and *dhx38*$^{-/-}$;*p53*$^{-/-}$ rescue the survival rate of *dhx38* mutants. Compared with *dhx38*$^{-/-}$ embryos, the survival ratios of *dhx38*$^{-/-}$ embryos incubated with PFT-β at 72 hpf (**P=0.003) and 76 hpf (*P=0.079) are significant. Compared with *dhx38*$^{-/-}$ embryos, the survival ratios of *dhx38*$^{-/-}$;*p53*$^{-/-}$ at 72 hpf (*P=0.012), 76 hpf (*P=0.029) and 80 hpf (**P=0.007) are significant. $n \geq 20$ per group. Experiments were performed with three replicates; (G-J) Quantification of cells from C-E. Data show the mean±s.d. Significance was determined with two-tailed unpaired Student's *t*-test. *P<0.05; **P<0.01; ***P<0.001; ****P<0.0001. All scale bars: 200 µm.

the Kupffer cells in the liver, Langerhans cells in the epidermis and alveolar macrophages in the lungs. Impaired EMP differentiation caused by *dhx38* deletion may result in the loss of the tissue-resident macrophage pool in adults, leading to related diseases.

Previously, we demonstrated that the splicing factor Bcas2 is vital for HSPC maintenance by regulating P53 signaling to inhibit apoptosis (Yu et al., 2019). Here, we report that the deletion of the splicing factor Dhx38 inhibits cell cycle progression and

Development (2022) 149, dev200450. doi:10.1242/dev.200450

differentiation of EMPs and HSPCs, and increases apoptosis in a P53-dependent-manner. These defective phenotypes observed in EMPs overlapped with those of HSPCs, pointing to common mechanisms underlying their development and maintenance.

As both EMPs and HSPCs exhibit hematopoietic progenitor cell characteristics, they are likely to have similar pathogenic mechanisms but also have distinct regulatory preferences. Of note, EMPs with fetal characteristics are developmentally restricted, but can be used for long-term multilineage reconstitution upon transplantation into adult recipients (Chen et al., 2011). This hematological model can serve as a useful model for understanding the temporal and spatial control of EMPs and HSPCs and the etiology of hematopoietic malignancies, and for facilitating the development and testing of novel therapeutic interventions.

Mitotic disorders affected by splicing factor dysfunction could be caused by the direct regulation of mitosis by these splicing factors or an indirect consequence of compromised splicing in cells. Previous studies have revealed that mutation of DHX38 affects the function of Aurora B and centromeric heterochromatin, which results in defective chromosome segregation in the mitotic phase (Nishimura et al., 2019; Vijayakumari et al., 2019). However, only a limited number of genes have been characterized as the targets of DHX38 in these studies. Our study is the first to elucidate the role of the splicing factor Dhx38 in regulating mitosis and differentiation by alternative splicing during hematopoiesis. As RNA splicing is often tissue specific, it is plausible that the Dhx38-regulated program in EMPs and HSPCs differs from that of other tissues. Here, we found that deletion of *dhx38* causes mitosis arrest in EMPs and HSPCs, accompanied by a 'grape' karyotype due to the defects in chromosome alignment. RNA-seq analysis identified abnormally spliced genes regulated by Dhx38, which are related to chromosome segregation, the microtubule cytoskeleton, cell cycle kinases and DNA damage (Fig. 6C,D). Although molecular mechanisms of how each process affects the mitosis of EMPs and HSPCs are currently unknown, it is likely that multiple regulatory mechanisms of Dhx38 co-exist in cells and work together to regulate the cell cycle.

In addition to regulating mitosis, deletion of *dhx38* leads to a shorter S phase and increased DNA damage in EMPs and HSPCs, implying an important role for Dhx38 in the maintenance of genomic integrity during DNA replication. Splicing-factor depletion could affect DNA replication during S phase, resulting in R-loop formation and associated genomic instability, which activates the DNA damage response (Chakraborty et al., 2018). Mitotic errors, such as lagging chromosomes, and mitotic delay can also cause DNA damage, which can trigger P53-dependent apoptosis (Edwards et al., 2021; Ganem and Pellman, 2012; Hayashi and Karlseder, 2013; Jelluma and Kops, 2014). A defective DNA damage response can lead to genomic instability underlying many diseases, including hematological disorders and cancer (Bugai et al., 2019; Yoshioka et al., 2021). The interplay between cell cycle inhibition, DNA damage and apoptosis is complex, and how these processes affect each other in *dhx38* mutants is unknown; thus, further investigation is required.

In summary, the most striking result to emerge from the data is the new insight into the role of Dhx38 in maintaining differentiation and survival of EMPs and HSPCs, by regulating pre-mRNA splicing of genes involved in mitosis. We hypothesize that mutation of splicing factors in cells with high proliferative requirements, including hematopoietic progenitors, neural progenitors or retinal progenitors, may share similar phenotypes. Mutations of splicing factors in acute myeloid leukemia and related myeloid malignancies have been confirmed; thus, this study contributes to our understanding of the potential role of altered pre-mRNA splicing in the pathogenesis of clonal hematopoietic malignancies.

MATERIAL AND METHODS

Fish strains and embryos

Zebrafish embryos were reared and kept at 28.5°C under standard aquaculture conditions, as described previously (Hu et al., 2019). Female and male zebrafish of the AB strain under 1 year of age were used. The transgenic zebrafish used in this study included Tg(*cmyb*:eGFP) (CZ273), Tg(*gata1*:dsred) (CZ64), Tg(*flk*:mCherry), Tg(*pu.1*-gal4-vp16-uas-GFP) (CZ83) and Tg(*mpeg1*:eGFP) (CZ98), and were purchased from the China Zebrafish Resource Center. Tg(*mpx*:eGFP) was obtained from Prof. Yiyue Zhang, South China University of Technology (Lian et al., 2018). All animal experimental procedures were reviewed and approved by the Ethics Committee of Huazhong University of Science and Technology.

Generation of *dhx38* mutants using CRISPR/Cas9 technology

dhx38$^{-/-}$ zebrafish were generated by CRISPR/Cas9 technology as described previously (Li et al., 2021). The guide RNAs (gRNAs) were designed by CHOPCHOP (http://chopchop.cbu.uib.no/). mMESSAGE mMACHINE T7 Transcription Kit (Invitrogen) and TranscriptAid T7 High Yield Transcription Kit (Thermo Fisher Scientific) were used to generate Cas9 mRNA and gRNAs, respectively. Zebrafish carrying *dhx38* mutations were identified by Sanger sequencing. The *dhx38* knockout zebrafish lines generated in this study have been deposited in the China Zebrafish Resource Center (CZRC).

RNA-seq

Total RNA from the trunk region of siblings and *dhx38*$^{-/-}$ embryos at 36 hpf was extracted using Trizol (Invitrogen). Using the Nanodrop and the Bioanalyzer 2100 (Agilent), RNA sample quality and quantity were assessed. Beijing Novogene and Biomarker used an Illumina HiSeq2000 platform to carry out RNA-seq. RNA-seq quality control and filtering were conducted using fastp software (https://github.com/OpenGene/fastp). Input files following quality control were aligned to the Zebrafish genome (Ensembl GRCz11) by STAR software using the two-pass strategy (Dobin and Gingeras, 2015). Gene expression data were extracted using featureCounts software (Liao et al., 2014) and differential analysis was performed using edgeR (Robinson et al., 2010) (Tables S1 and S2). Alternative splicing analysis was implemented by the software rMATS (Shen et al., 2014) and visualized using rmats2sashimiplot (https://github.com/Xinglab/rmats2sashimiplot) for significant differential splicing events (Tables S3 and S4; Fig. S7) (Li et al., 2021). Metascape (http://metascape.org) was used to identify Gene Ontology terms enriched in the differentially expressed genes and differentially spliced genes (Tables S1 and S2). RNA-seq data in this study have been uploaded to the Gene Expression Omnibus under the accession number GSE165203.

WISH

WISH for zebrafish embryos was performed as described previously (Yu et al., 2019). More than 40 zebrafish embryos were used to ensure that the proportion of homozygous embryos was above 10. The genes examined using RNA *in situ* hybridization included *scl*, *gata1*, *pu.1*, *cmyb*, *lmo2*, *dll4*, *dab2*, *hbae1*, *lcp1*, *lyz*, *cebpa*, *mpeg1*, *mpx*, *hbbe1.1*, *dhx38*, *mfap4* and *rag1*. The primers used to synthesize the probes are listed in Table S5.

Semi-qPCR and qRT-PCR

Semi-qPCR was performed to confirm abnormal alternative splicing. Primers were designed for differentially spliced genes with aberrant splice sites. The PCR products were analyzed by gel electrophoresis and visualized using the gel ultraviolet detector ZF-401 (Shanghai Guanghao Analytical Instrument). PSI values from 0 to 100 reflected the ratio of correct splicing from the total junction reads (Li et al., 2021). Exons/introns that are constitutively retained in all transcripts and are never skipped have a PSI of 100.

qRT-PCR was conducted with AceQ qPCR SYBR Green Master Mix (Vazyme Biotech) in a StepOnePlus real-time PCR machine (Applied Biosystems). Gene expression was normalized to *gapdh*. The primers for semi-qPCR and qRT-PCR are summarized in Table S5.

Development (2022) 149, dev200450. doi:10.1242/dev.200450

Sudan Black staining

To prepare the staining solution, 0.3 g of Sudan Black (4197-25-5, Sigma-Aldrich) was added to 100 ml of anhydrous ethanol (64-17-5, Sinopharm) and heated or ground for 1-2 days to dissolve completely. To prepare the buffer solution, 16 g of crystalline phenol (108-95-2, Sigma-Aldrich) dissolved in 30 ml of anhydrous ethanol was added to 100 ml of water containing 0.3 g of sodium dihydrogen phosphate (7558-80-7, Sinopharm). These solutions were stored at 4°C and used immediately after mixing the staining solution and buffer solution in a 3:2 ratio. The fixed embryos were incubated in 1 ml Sudan Black staining solution (mixed solution) for 20 min, then washed with 70% ethanol and photographed under the Nikon Eclipse 80i Advanced Research Microscope (Nikon, RRID:SCR_015572).

Neutral Red staining

Neutral Red can be phagocytosed by macrophages and concentrated in their lysosomes, thus causing live macrophages to be labeled red. To prepare the Neutral Red solution, 0.01 g of Neutral Red powder was dissolved in 1 ml of pure water, and the completely dissolved Neutral Red (10 mg/ml) was stored at 4°C and protected from light. Live embryos at 36 hpf were incubated in 1 ml of Neutral Red staining solution (2.5 µg/ml) at 28°C for 8 h and protected from light. Embryos were washed three times in PBS with 0.1% Triton X-100 (PBST) for 5 min each, fixed with 4% paraformaldehyde (PFA) and photographed by Eclipse 80i (Nikon).

P53 inhibitor treatment

Zebrafish embryos were incubated with 1 µM PFT-β (0477-34-1, MedChemExpress) from 12 hpf. The number of zebrafish was counted and genotyped daily to supervise the survival rate.

Immunofluorescence, TUNEL staining and EdU assay

Embryos were collected and fixed with 4% PFA overnight at 4°C. After washing with PBST, embryos were soaked in acetone for 15 min. Embryos were then blocked with PBST containing 10% goat serum at room temperature for 1 h. After blocking, embryos were incubated with the primary antibody overnight at 4°C. The fluorescent dye-conjugated secondary antibody was used to visualize the signals. The primary and secondary antibodies used are listed in Table S6. The immunofluorescence signals were observed and imaged using an FV1000 confocal microscope (Olympus, RRID:SCR_020337).

TUNEL staining was performed using the TUNEL BrightRed/Green Apoptosis Detection Kit (A113/A112, Vazyme). For the EdU assay, live embryos at 34 hpf were incubated in EdU (2 mM) for 30 min at 4°C and then switched to fresh water for 2 h. Embryos were then fixed with 4% PFA overnight at 4°C, and apoptotic cells were detected by the Cell-Light EdU Apollo567/488 *in vitro* Kit (C10310/C10338, RiboBio, Guangzhou, China). Images were taken with a Nikon Eclipse 80i Advanced Research Microscope (Nikon, RRID:SCR_015572).

Cell culture and flow analysis

The K562 cell line was obtained from Prof. Yong You's lab (Huazhong University of Science and Technology) and tested for contamination (Zhou et al., 2021). siRNAs targeting different coding regions of human DHX38 were designed by RiboBio . Two independent siRNAs were used for the *DHX38* gene to avoid off-target effects. The siDHX38-641 RNA is at the c.641 position of the human *DHX38* gene, and siDHX38-328 is at c.328. A nonspecific siRNA duplex was used as an siRNA negative control (si-NC). The silencing effects of these two siRNAs were confirmed by western blotting. The sequences of the siRNAs used in this study are listed in Table S7. K562 cells were transfected with DHX38 siRNA using Lipofectamine 3000 (Invitrogen) according to the manufacturer's protocol. After 72 h, suspension cells were collected and washed with cold PBS. Cells were then resuspended in 700 µl of PBS with 300 µl of 70% ice-cold ethanol slowly added on a gentle shaker. Cells were then fixed overnight in the freezer at −20°C. After washing the cells with PBS, 1 ml of propidium iodide solution (at a final concentration of 20 µg/ml propidium iodide, containing 0.1% Triton X-100 and 0.2 mg/ml RNase A) was added, the cells were evenly dispersed and stained for at least 30 min protected from light. Analysis was performed on Cytoflex S (Beckman Coulter, RRID: SCR_019627) and cell cycle calculations were performed with FlowJo software (https://www.flowjo.com/) using the Dean–Jett–Fox model (RRID:SCR_008520).

Statistical analysis

For statistical analysis, data are represented as mean±s.d., and a statistically significant difference between control and experimental groups was determined by an unpaired, two-tailed Student's *t*-test. The level of significance was set to $P<0.05$.

Acknowledgements

The authors would like to thank Dr Feng Liu, University of Chinese Academy of Sciences, for advising on this paper, Dr Yiyue Zhang, South China University of Technology, for providing transgene fluorescence zebrafish and commenting on this paper, and Dr Yong You, Huazhong University of Science and Technology, for providing K562 cells.

Competing interests

The authors declare no competing or financial interests.

Author contributions

Conceptualization: J.T., S.Y., M.L.; Methodology: J.T., J. Li, K.S., Y.L., Y. Han; Software: Y.Z.; Formal analysis: Y. Han, Y. Huang; Investigation: X.R.; Resources: J. Li, K.S., Z.T.; Data curation: J.T., S.Y., M.R., J. Luo; Writing - original draft: J.T.; Writing - review & editing: S.Y., X.R., T.J., M.T.S.W.; Supervision: Z.T., Q.L., M.L.; Project administration: Q.L., M.L.; Funding acquisition: Q.L., M.L.

Funding

This work was supported by grants from the Ministry of Science and Technology of the People's Republic of China (2018YFA0801000), and the National Natural Science Foundation of China (82071010, 81670099, 81800870, 31801041 and 81870691).

Data availability

RNA-sequencing data from this study have been deposited in the Gene Expression Omnibus under the accession number GSE165203. The raw data underlying graphs and charts, including uncropped versions of gels and western blots, have been deposited in Mendeley (https://doi.org/10.17632/x5g6kf96vg.1).

Peer review history

The peer review history is available online at https://journals.biologists.com/dev/lookup/doi/10.1242/dev.200450.reviewer-comments.pdf

References

Baeten, J. T. and de Jong, J. L. O. (2018). Genetic models of leukemia in zebrafish. *Front. Cell Dev. Biol.* **6**, 115. doi:10.3389/fcell.2018.00115

Baralle, F. E. and Giudice, J. (2017). Alternative splicing as a regulator of development and tissue identity. *Nat. Rev. Mol. Cell Biol.* **18**, 437-451. doi:10.1038/nrm.2017.27

Bertrand, J. Y., Kim, A. D., Violette, E. P., Stachura, D. L., Cisson, J. L. and Traver, D. (2007). Definitive hematopoiesis initiates through a committed erythromyeloid progenitor in the zebrafish embryo. *Development* **134**, 4147-4156. doi:10.1242/dev.012385

Bertrand, J. Y., Kim, A. D., Teng, S. and Traver, D. (2008). CD41+ cmyb+ precursors colonize the zebrafish pronephros by a novel migration route to initiate adult hematopoiesis. *Development* **135**, 1853-1862. doi:10.1242/dev.015297

Bertrand, J. Y., Cisson, J. L., Stachura, D. L. and Traver, D. (2010). Notch signaling distinguishes 2 waves of definitive hematopoiesis in the zebrafish embryo. *Blood* **115**, 2777-2783. doi:10.1182/blood-2009-09-244590

Bugai, A., Quaresma, A. J. C., Friedel, C. C., Lenasi, T., Duster, R., Sibley, C. R., Fujinaga, K., Kukanja, P., Hennig, T., Blasius, M. et al. (2019). P-TEFb Activation by RBM7 Shapes a Pro-survival Transcriptional Response to Genotoxic Stress. *Mol. Cell* **74**, 254-267.e10. doi:10.1016/j.molcel.2019.01.033

Calzetta, N. L., González Besteiro, M. A. and Gottifredi, V. (2020). Mus81-Eme1-dependent aberrant processing of DNA replication intermediates in mitosis impairs genome integrity. *Sci. Adv.* **6**, eabc8257. doi:10.1126/sciadv.abc8257

Carvalhal, S., Ribeiro, S. A., Arocena, M., Kasciukovic, T., Temme, A., Koehler, K., Huebner, A. and Griffis, E. R. (2015). The nucleoporin ALADIN regulates Aurora A localization to ensure robust mitotic spindle formation. *Mol. Biol. Cell* **26**, 3424-3438. doi:10.1091/mbc.E15-02-0113

Carvalho, C. A., Moreira, S., Ventura, G., Sunkel, C. E. and Morais-de-Sá, E. (2015). Aurora A triggers Lgl cortical release during symmetric division to control planar spindle orientation. *Curr. Biol.* **25**, 53-60. doi:10.1016/j.cub.2014.10.053

Chakraborty, P., Huang, J. T. J. and Hiom, K. (2018). DHX9 helicase promotes R-loop formation in cells with impaired RNA splicing. *Nat. Commun.* **9**, 4346. doi:10.1038/s41467-018-06677-1
Cheeseman, I. M., Hori, T., Fukagawa, T. and Desai, A. (2008). KNL1 and the CENP-H/I/K complex coordinately direct kinetochore assembly in vertebrates. *Mol. Biol. Cell* **19**, 587-594. doi:10.1091/mbc.e07-10-1051
Chen, T.-C., Lee, S.-A., Chan, C.-H., Juang, Y.-L., Hong, Y.-R., Huang, Y.-H., Lai, J.-M., Kao, C.-Y. and Huang, C.-Y. F. (2009). Cliques in mitotic spindle network bring kinetochore-associated complexes to form dependence pathway. *Proteomics* **9**, 4048-4062. doi:10.1002/pmic.200900231
Chen, M. J., Li, Y., De Obaldia, M. E., Yang, Q., Yzaguirre, A. D., Yamada-Inagawa, T., Vink, C. S., Bhandoola, A., Dzierzak, E. and Speck, N. A. (2011). Erythroid/myeloid progenitors and hematopoietic stem cells originate from distinct populations of endothelial cells. *Cell Stem Cell* **9**, 541-552. doi:10.1016/j.stem.2011.10.003
Chen, L., Kostadima, M., Martens, J. H. A., Canu, G., Garcia, S. P., Turro, E., Downes, K., Macaulay, I. C., Bielczyk-Maczynska, E., Coe, S. et al. (2014). Transcriptional diversity during lineage commitment of human blood progenitors. *Science* **345**, 1251033. doi:10.1126/science.1251033
Da'as, S. I., Coombs, A. J., Balci, T. B., Grondin, C. A., Ferrando, A. A. and Berman, J. N. (2012). The zebrafish reveals dependence of the mast cell lineage on Notch signaling in vivo. *Blood* **119**, 3585-3594. doi:10.1182/blood-2011-10-385989
Dai, Y. M., Zhu, L., Huang, Z. B., Zhou, M. Y., Jin, W., Liu, W., Xu, M. C., Yu, T., Zhang, Y. Y., Wen, Z. L. et al. (2016). Cebpα is essential for the embryonic myeloid progenitor and neutrophil maintenance in zebrafish. *J. Genet. Genomics* **43**, 593-600. doi:10.1016/j.jgg.2016.09.001
Danilova, N., Kumagai, A. and Lin, J. (2010). p53 upregulation is a frequent response to deficiency of cell-essential genes. *PLoS One* **5**, e15938. doi:10.1371/journal.pone.0015938
De La Garza, A., Cameron, R. C., Nik, S., Payne, S. G. and Bowman, T. V. (2016). Spliceosomal component Sf3b1 is essential for hematopoietic differentiation in zebrafish. *Exp. Hematol.* **44**, 826-837.e4. doi:10.1016/j.exphem.2016.05.012
Dege, C., Fegan, K. H., Creamer, J. P., Berrien-Elliott, M. M., Luff, S. A., Kim, D., Wagner, J. A., Kingsley, P. D., McGrath, K. E., Fehniger, T. A. et al. (2020). Potently cytotoxic natural killer cells initially emerge from erythro-myeloid progenitors during mammalian development. *Dev. Cell* **53**, 229-239.e7. doi:10.1016/j.devcel.2020.02.016
Dobin, A. and Gingeras, T. R. (2015). Mapping RNA-seq Reads with STAR. *Curr. Protoc. Bioinformatics* **51**, 11.14.1-11.14.19. doi:10.1002/0471250953.bi1114s51
Edwards, D. M., Mitchell, D. K., Abdul-Sater, Z., Chan, K.-K., Sun, Z., Sheth, A., He, Y., Jiang, L., Yuan, J., Sharma, R. et al. (2021). Mitotic errors promote genomic instability and leukemia in a novel mouse model of Fanconi anemia. *Front. Oncol.* **11**, 752933. doi:10.3389/fonc.2021.752933
Fica, S. M., Oubridge, C., Galej, W. P., Wilkinson, M. E., Bai, X.-C., Newman, A. J. and Nagai, K. (2017). Structure of a spliceosome remodelled for exon ligation. *Nature* **542**, 377-380. doi:10.1038/nature21078
Forrester, A. M., Berman, J. N. and Payne, E. M. (2012). Myelopoiesis and myeloid leukaemogenesis in the zebrafish. *Adv. Hematol.* **2012**, 358518. doi:10.1155/2012/358518
Frame, J. M., Fegan, K. H., Conway, S. J., McGrath, K. E. and Palis, J. (2016). Definitive hematopoiesis in the yolk sac emerges from Wnt-responsive hemogenic endothelium independently of circulation and arterial identity. *Stem Cells* **34**, 431-444. doi:10.1002/stem.2213
Ganem, N. J. and Pellman, D. (2012). Linking abnormal mitosis to the acquisition of DNA damage. *J. Cell Biol.* **199**, 871-881. doi:10.1083/jcb.201210040
Gatti, M., Imhof, R., Huang, Q., Baudis, M. and Altmeyer, M. (2020). The ubiquitin ligase TRIP12 limits PARP1 trapping and constrains PARP inhibitor efficiency. *Cell Rep.* **32**, 107985. doi:10.1016/j.celrep.2020.107985
Gong, D. and Ferrell, J. E. (2010). The roles of cyclin A2, B1, and B2 in early and late mitotic events. *Mol. Biol. Cell* **21**, 3149-3161. doi:10.1091/mbc.e10-05-0393
Gottgens, B., Broccardo, C., Sanchez, M. J., Deveaux, S., Murphy, G., Göthert, J. R., Kotsopoulou, E., Kinston, S., Delaney, L., Piltz, S. et al. (2004). The scl +18/19 stem cell enhancer is not required for hematopoiesis: identification of a 5' bifunctional hematopoietic-endothelial enhancer bound by Fli-1 and Elf-1. *Mol. Cell. Biol.* **24**, 1870-1883. doi:10.1128/MCB.24.5.1870-1883.2004
Han, S., Park, J. and Lee, D. H. (2015). Protein DHX38 is a novel inhibitor of protein phosphatase 4. *Anim. Cells Syst.* **19**, 236-244. doi:10.1080/19768354.2015.1074106
Hayashi, M. T. and Karlseder, J. (2013). DNA damage associated with mitosis and cytokinesis failure. *Oncogene* **32**, 4593-4601. doi:10.1038/onc.2012.615
Hoeffel, G., Chen, J., Lavin, Y., Low, D., Almeida, F. F., See, P., Beaudin, A. E., Lum, J., Low, I., Forsberg, E. C. et al. (2015). C-Myb+ erythro-myeloid progenitor-derived fetal monocytes give rise to adult tissue-resident macrophages. *Immunity* **42**, 665-678. doi:10.1016/j.immuni.2015.03.011
Holdgaard, S. G., Cianfanelli, V., Pupo, E., Lambrughi, M., Lubas, M., Nielsen, J. C., Eibes, S., Maiani, E., Harder, L. M., Wesch, N. et al. (2019). Selective autophagy maintains centrosome integrity and accurate mitosis by turnover of centriolar satellites. *Nat. Commun.* **10**, 4176. doi:10.1038/s41467-019-12094-9
Hong, E., Jayachandran, P. and Brewster, R. (2010). The polarity protein Pard3 is required for centrosome positioning during neurulation. *Dev. Biol.* **341**, 335-345. doi:10.1016/j.ydbio.2010.01.034
Hsia, D. A., Tepper, C. G., Pochampalli, M. R., Hsia, E. Y., Izumiya, C., Huerta, S. B., Wright, M. E., Chen, H. W., Kung, H. J. and Izumiya, Y. (2010). KDM8, a H3K36me2 histone demethylase that acts in the cyclin A1 coding region to regulate cancer cell proliferation. *Proc. Natl. Acad. Sci. USA* **107**, 9671-9676. doi:10.1073/pnas.1000401107
Hu, X., Lu, Z., Yu, S., Reilly, J., Liu, F., Jia, D., Qin, Y., Han, S., Liu, X., Qu, Z. et al. (2019). CERKL regulates autophagy via the NAD-dependent deacetylase SIRT1. *Autophagy* **15**, 453-465. doi:10.1080/15548627.2018.1520548
Huang, L., Meng, T.-G., Ma, X.-S., Wang, Z.-B., Qi, S.-T., Chen, Q., Zhang, Q.-H., Liang, Q.-X., Wang, Z.-W., Hu, M.-W. et al. (2019). Rad9a is involved in chromatin decondensation and post-zygotic embryo development in mice. *Cell Death Differ.* **26**, 969-980. doi:10.1038/s41418-018-0181-9
Jelluma, N. and Kops, G. J. (2014). Collateral genome instability by DNA damage in mitosis. *Cancer Discov.* **4**, 1256-1258. doi:10.1158/2159-8290.CD-14-1097
Latif, Z., Chakchouk, I., Schrauwen, I., Lee, K., Santos-Cortez, R. L. P., Abbe, I., Acharya, A., Jarral, A., Ali, I., Ullah, E. et al. (2018). Confirmation of the role of DHX38 in the etiology of early-onset retinitis pigmentosa. *Invest. Ophthalmol. Vis. Sci.* **59**, 4552-4557. doi:10.1167/iovs.18-23849
Li, D., Xue, W., Li, M., Dong, M., Wang, J., Wang, X., Li, X., Chen, K., Zhang, W., Wu, S. et al. (2018a). VCAM-1(+) macrophages guide the homing of HSPCs to a vascular niche. *Nature* **564**, 119-124. doi:10.1038/s41586-018-0709-7
Li, Z., Liu, S., Xu, J., Zhang, X., Han, D., Liu, J., Xia, M., Yi, L., Shen, Q., Xu, S. et al. (2018b). Adult connective tissue-resident mast cells originate from late Erythro-myeloid progenitors. *Immunity* **49**, 640-653.e5. doi:10.1016/j.immuni.2018.09.023
Li, J., Liu, F., Lv, Y., Sun, K., Zhao, Y., Reilly, J., Zhang, Y., Tu, J., Yu, S., Liu, X. et al. (2021). Prpf31 is essential for the survival and differentiation of retinal progenitor cells by modulating alternative splicing. *Nucleic Acids Res.* **49**, 2027-2043. doi:10.1093/nar/gkab003
Lian, J. W., Chen, J. K., Wang, K., Zhao, L. F., Meng, P., Yang, L. T., Wei, J. Y., Ma, N., Xu, J., Zhang, W. Q. et al. (2018). Alas1 is essential for neutrophil maturation in zebrafish. *Haematologica* **103**, 1785-1795. doi:10.3324/haematol.2018.194316
Liao, Y., Smyth, G. K. and Shi, W. (2014). featureCounts: an efficient general purpose program for assigning sequence reads to genomic features. *Bioinformatics* **30**, 923-930. doi:10.1093/bioinformatics/btt656
Ma, Y., Barnett, T., Chai, L., Yang, J. C., Alipio, Z., Pei, L., Amin, H. M., Fink, L., Di, C. H. and Yan, H. (2006). DEAH-box splicing factor gene, prp16 amplification in acute myeloid leukemia. *Blood* **108**, 198. doi:10.1182/blood.V108.11.198.198
Mass, E., Jacome-Galarza, C. E., Blank, T., Lazarov, T., Durham, B. H., Ozkaya, N., Pastore, A., Schwabenland, M., Chung, Y. R., Rosenblum, M. K. et al. (2017). A somatic mutation in erythro-myeloid progenitors causes neurodegenerative disease. *Nature* **549**, 389-393. doi:10.1038/nature23672
McGrath, K. E., Frame, J. M., Fromm, G. J., Koniski, A. D., Kingsley, P. D., Little, J., Bulger, M. and Palis, J. (2011). A transient definitive erythroid lineage with unique regulation of the beta-globin locus in the mammalian embryo. *Blood* **117**, 4600-4608. doi:10.1182/blood-2010-12-325357
Medina-Pritchard, B., Lazou, V., Zou, J., Byron, O., Abad, M. A., Rappsilber, J., Heun, P. and Jeyaprakash, A. A. (2020). Structural basis for centromere maintenance by Drosophila CENP-A chaperone CAL1. *EMBO J.* **39**, e103234. doi:10.15252/embj.2019103234
Nishimura, K., Cho, Y., Tokunaga, K., Nakao, M., Tani, T. and Ideue, T. (2019). DEAH box RNA helicase DHX38 associates with satellite I noncoding RNA involved in chromosome segregation. *Genes Cells* **24**, 585-590. doi:10.1111/gtc.12707
Pellagatti, A. and Boultwood, J. (2020). Splicing factor mutant myelodysplastic syndromes: recent advances. *Adv. Biol. Regul.* **75**, 100655. doi:10.1016/j.jbior.2019.100655
Piwko, W., Mlejnkova, L. J., Mutreja, K., Ranjha, L., Stafa, D., Smirnov, A., Brodersen, M. M., Zellweger, R., Sturzenegger, A., Janscak, P. et al. (2016). The MMS22L-TONSL heterodimer directly promotes RAD51-dependent recombination upon replication stress. *EMBO J.* **35**, 2584-2601. doi:10.15252/embj.201593132
Robinson, M. D., McCarthy, D. J. and Smyth, G.K. (2010). edgeR: a Bioconductor package for differential expression analysis of digital gene expression data. *Bioinformatics* **26**, 139–140. doi:10.1093/bioinformatics/btp616
Sansam, C. L., Shepard, J. L., Lai, K., Ianari, A., Danielian, P. S., Amsterdam, A., Hopkins, N. and Lees, J. A. (2006). DTL/CDT2 is essential for both CDT1 regulation and the early G2/M checkpoint. *Genes Dev.* **20**, 3117-3129. doi:10.1101/gad.1482106
Shen, S., Park, J. W., Lu, Z. X., Lin, L., Henry, M. D., Wu, Y. N., Zhou, Q. and Xing, Y. (2014). rMATS: robust and flexible detection of differential alternative splicing from replicate RNA-Seq data. *Proc. Natl. Acad. Sci. USA* **111**, E5593-E5601. doi:10.1073/pnas.1419161111

Sudo, H. and Maru, Y. (2008). LAPSER1/LZTS2: a pluripotent tumor suppressor linked to the inhibition of katanin-mediated microtubule severing. *Hum. Mol. Genet.* **17**, 2524-2540. doi:10.1093/hmg/ddn153

Vijayakumari, D., Sharma, A. K., Bawa, P. S., Kumar, R., Srinivasan, S. and Vijayraghavan, U. (2019). Early splicing functions of fission yeast Prp16 and its unexpected requirement for gene Silencing is governed by intronic features. *RNA Biol.* **16**, 754-769. doi:10.1080/15476286.2019.1585737

Wang, L. Y. and Kung, H. J. (2012). Male germ cell-associated kinase is overexpressed in prostate cancer cells and causes mitotic defects via deregulation of APC/C-CDH1. *Oncogene* **31**, 2907-2918. doi:10.1038/onc.2011.464

Wehrkamp-Richter, S., Hyppa, R. W., Prudden, J., Smith, G. R. and Boddy, M. N. (2012). Meiotic DNA joint molecule resolution depends on Nse5-Nse6 of the Smc5-Smc6 holocomplex. *Nucleic Acids Res.* **40**, 9633-9646. doi:10.1093/nar/gks713

Weinreb, J. T., Ghazale, N., Pradhan, K., Gupta, V., Potts, K. S., Tricomi, B., Daniels, N. J., Padgett, R. A., De Oliveira, S., Verma, A. et al. (2021). Excessive R-loops trigger an inflammatory cascade leading to increased HSPC production. *Dev. Cell* **56**, 627-640.e5. doi:10.1016/j.devcel.2021.02.006

Xia, J., Kang, Z., Xue, Y., Ding, Y., Gao, S., Zhang, Y., Lv, P., Wang, X., Ma, D., Wang, L. et al. (2021). A single-cell resolution developmental atlas of hematopoietic stem and progenitor cell expansion in zebrafish. *Proc. Natl. Acad. Sci. USA* **118**, e2015748118. doi:10.1073/pnas.2015748118

Yokomizo, T., Mori, S., Kurokawa, M., Osato, M. and Komatsu, N. (2018). Hlf expression marks the developmental pathway for hematopoietic stem cells but not for erythroid-myeloid progenitors. *Cancer Sci.* **109**, 1093-1093. doi:10.1084/jem.20181399

Yoshioka, K. I., Kusumoto-Matsuo, R., Matsuno, Y. and Ishiai, M. (2021). Genomic instability and cancer risk associated with erroneous DNA repair. *Int. J. Mol. Sci.* **22**, 12254. doi:10.3390/ijms222212254

Yu, S., Jiang, T., Jia, D., Han, Y., Liu, F., Huang, Y., Qu, Z., Zhao, Y., Tu, J., Lv, Y. et al. (2019). BCAS2 is essential for hematopoietic stem and progenitor cell maintenance during zebrafish embryogenesis. *Blood* **133**, 805-815. doi:10.1182/blood-2018-09-876599

Zhang, Y., Gao, S., Xia, J. and Liu, F. (2018). Hematopoietic Hierarchy - An Updated Roadmap, *Trends Cell Biol.* **28**, 976-986. doi:10.1016/j.tcb.2018.06.001

Zhou, S., Li, W., Xiao, Y., Zhu, X., Zhong, Z., Li, Q., Cheng, F., Zou, P., You, Y. and Zhu, X. (2021). A novel chimeric antigen receptor redirecting T-cell specificity towards CD26+ cancer cells. *Leukemia* **35**, 119-129. doi:10.1038/s41375-020-0824-y

Zhu, X., Liang, Y. W., Gao, F. and Pan, J. M. (2017). IFT54 regulates IFT20 stability but is not essential for tubulin transport during ciliogenesis. *Cell. Mol. Life Sci.* **74**, 3425-3437. doi:10.1007/s00018-017-2525-x

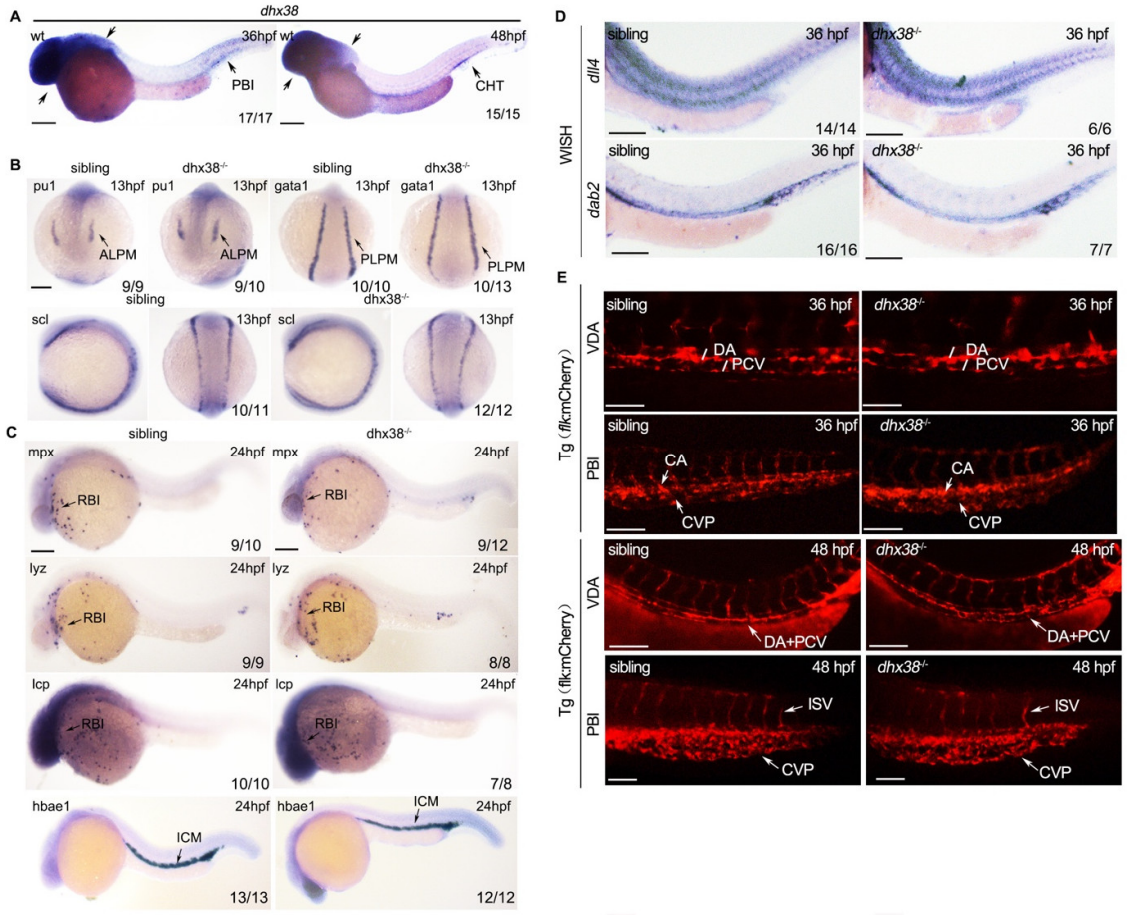

Fig. S1. Primary hematopoiesis and vascular development are unaffected in the *dhx38* mutants.

A WISH with a *dhx38* probe reflects *dhx38* expression in the PBI and CHT region at 36 hpf and 48 hpf, respectively. Black arrowheads indicate the expression pattern of *dhx38* markers. Scale bars, 200 μm. **B** Whole-mount in situ hybridization (WISH) was used to analyze the expression of the myeloid progenitor cell marker *pu.1*, the erythroid progenitor cell marker *gata1*, and the hemangioblastoma cells marker *scl* in siblings and *dhx38*$^{-/-}$ embryos at 13 hpf. Scale bars, 200 μm. C The expression of myeloid marker

mpx/*lyz*/*lcp* at the rostral blood island (RBI) and erythroid marker *hbae1* at the intermediate cell mass (ICM) is normal in the *dhx38* mutants at 24 hpf. Scale bars, 200 μm. **D** WISH detected the expression of the arterial marker *dll4* and the vein marker *dab2* in the *dhx38*$^{-/-}$ embryo is identical to that of siblings. Scale bars, 100 μm. **E** Fluorescence observation of *flk*$^{+}$ endothelium in Tg(*flk*:mCherry) shows that vascular development is generally normal at 36 hpf and 48 hpf in the *dhx38*$^{-/-}$ embryos. DA: dorsal aorta, PCV: posterior cardinal vein, CA: caudal artery, CVP: caudal venous plexus, ISV: intersegmental vessels, white line: DA diameter. Scale bars, 50 μm.

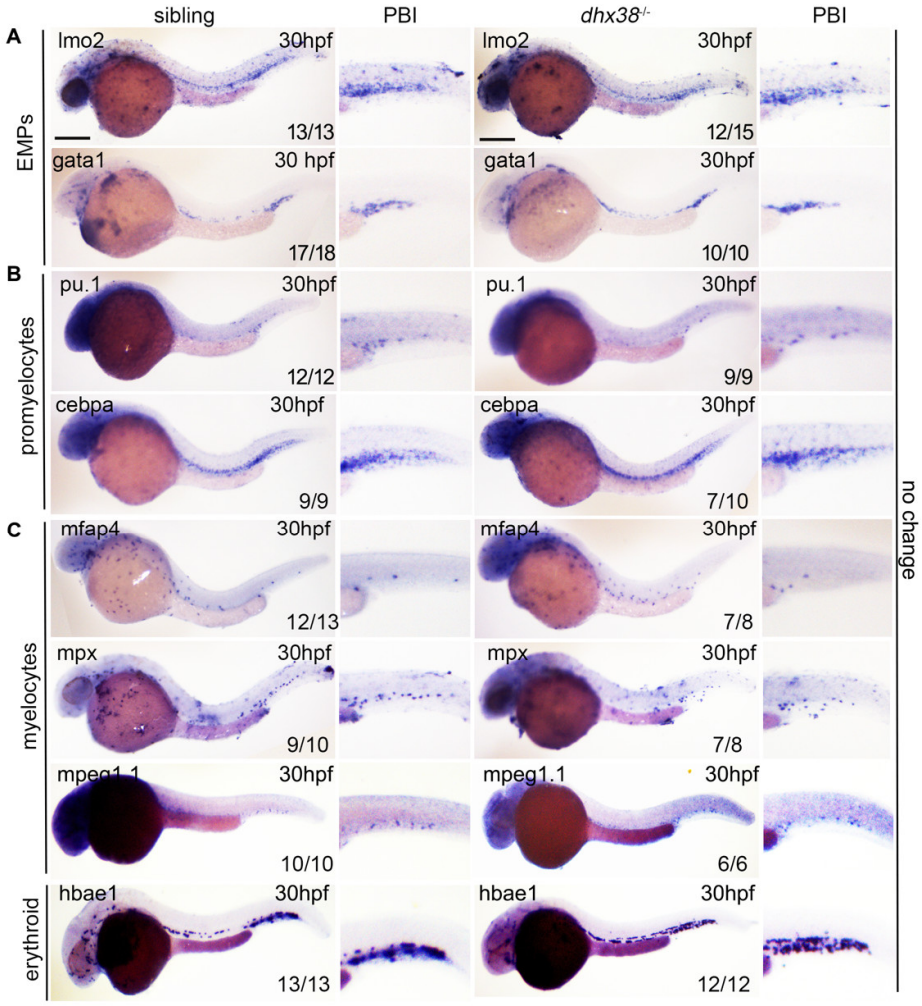

Fig. S2. EMP differentiation is normal in the *dhx38* mutant at 30hpf.

WISH results with *lmo2*, *gata1*, *pu.1*, *cebpa*, *mfap4*, *mpx*, *mpeg1.1* and *hbae1* probes demonstrate that EMP development in *dhx38* mutant is identical to that of wild-type siblings. Scale bars, 200 μm.

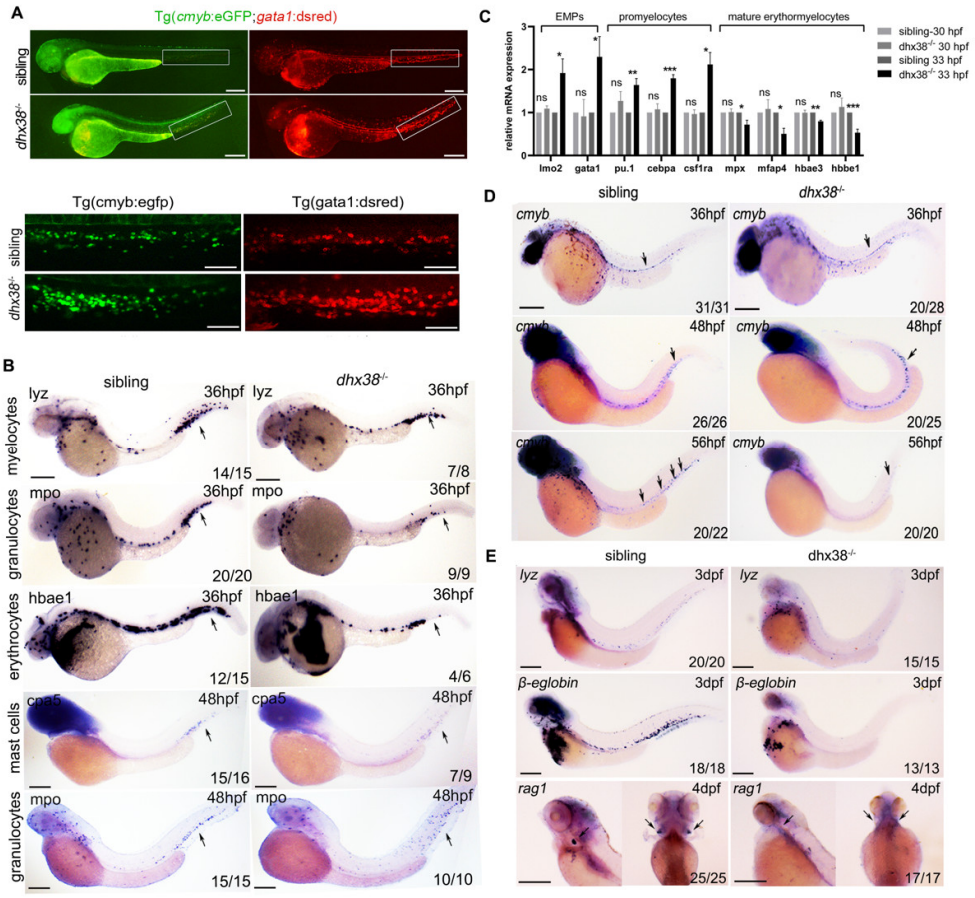

Fig. S3. Loss of *dhx38* impairs EMP differentiation.

A Whole embryo of Tg(*cmyb*:eGFP;*gata1*:dsred) shows increased EMPs at 36 hpf. Scale bars, 1 mm. With enlarged view in PBI region of the whole embryo. Scale bars, 50 μm. **B** WISH detected the expression of *lyz*, *mpo*, *hbae1* which are significantly decreased in *dhx38*$^{-/-}$ zebrafish at 36 hpf. Scale bars, 200 μm. WISH detected the expression of *cpa5* and *mpo* showing that mature myeloid cells are decreased in *dhx38*$^{-/-}$ zebrafish at 48 hpf. The black arrow indicated the CHT region of the zebrafish. Scale bars, 200 μm. **C** qRT-PCR analysis of genes related to EMP differentiation process in embryos at 30 hpf and 33 hpf. The EMPs specific genes *lmo2*, *gata1* and promyelocytes genes *pu.1*, *cebpa*, *csf1ra* are elevated, however mature erythromyelocyte marker genes (*mpx, mfap4, hbae3, hbae1*) are decreased

at 33 hpf. n ≥ 12 per group, performed with three replicates; internal control, GAPDH; two-tailed Student's t-test, *p < 0.05, **p < 0.01, ***p < 0.001, ****p < 0.0001; error bars, mean ± SD. **D** The expression of the hematopoietic progenitor cell marker *cmyb* at 36 hpf, 48 hpf and 56 hpf in siblings and *dhx38* mutants. The black arrows indicate the position of the *cmyb* gene expression. Scale bars, 200 μm. **E** WISH analyzed the expression of the myeloid marker *lyz*, and the erythroid marker *β-eglobin* (*hbae1*), and the lymphoid marker *rag1* in *dhx38* mutants and wild-type siblings. Black arrows indicated the position of marker gene expression. Scale bars, 200 μm.

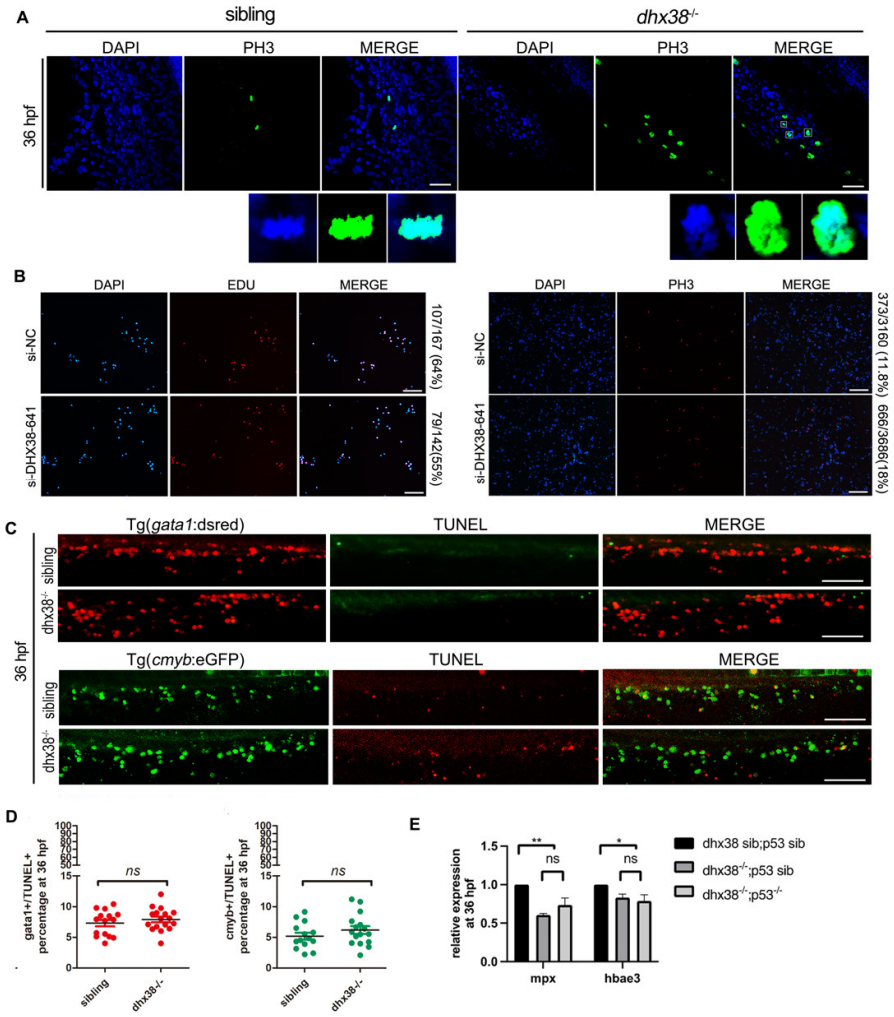

Fig. S4. *Dhx38* mutants exhibit disordered mitosis.

A Confocal image of immunostaining by DAPI and pH3 shows that pH3+ cells exhibit an abnormal karyotype in the *dhx38* mutants. Scale bars, 50 μm. **B** EdU assay shows a reduction of cells in S-phase from 64% to 55% in K562 cells following treatment with si-DHX38-641. Scale bars, 50 μm. pH3 immunostaining shows an increasement of cells in M- phase numbers from 11% to 18% in K562 cells following treatment with si-DHX38-641. Scale bars, 50 μm. **C** TUNEL staining shows that the proportion of apoptotic EMPs and HSPCs in *dhx38*$^{-/-}$ embryos are identical to that of siblings at 36 hpf. **D** The double-positive fluorescence in the PBI show that EMPs and HSPCs are undergoing apoptosis. Scale bars, 100 μm. **E** Although *p53* expression is increased in the mutants' CHT at 36 hpf, inhibiting *p53* activity in *dhx38* mutants failed to rescue the phenotype of granulocyte (*mpx*) and erythrocyte (*hbae3*) reduction at 36 hpf.

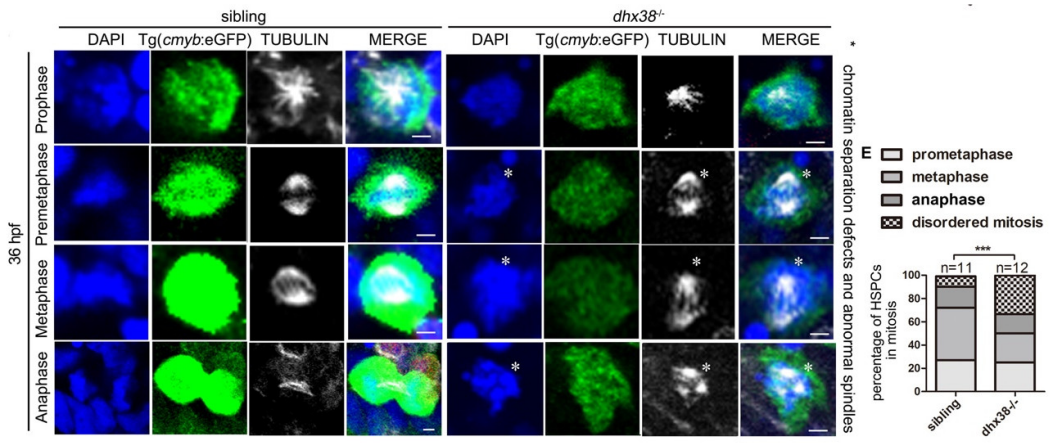

Fig. S5. HSPCs from *dhx38* mutants exhibit disordered mitosis.

Confocal image of three-color immunostaining by cmyb (green), DAPI (blue) and α-TUBULIN (white) at 36 hpf. HSPCs (*cmyb*+) from dhx38 mutants exhibiting disordered mitosis. Asterisks represents abnormal mitotic processes. Scale bars, 5 μm. The statistics of HSPC mitosis.

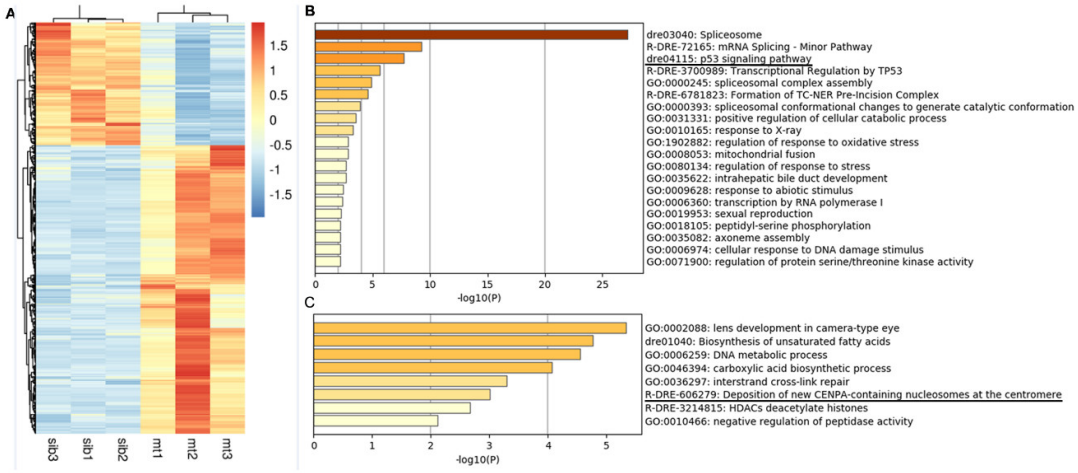

Fig. S6. Differentially expressed genes in the *dhx38* mutants.

A Heat map of differentially expressed genes. **B** GO enrichment map of up-regulated differentially expressed genes, black lines represent phenotypes associated with P53 signaling. **C** GO enrichment map of down-regulated differentially expressed genes, black lines represent phenotypes associated with chromosome segregation.

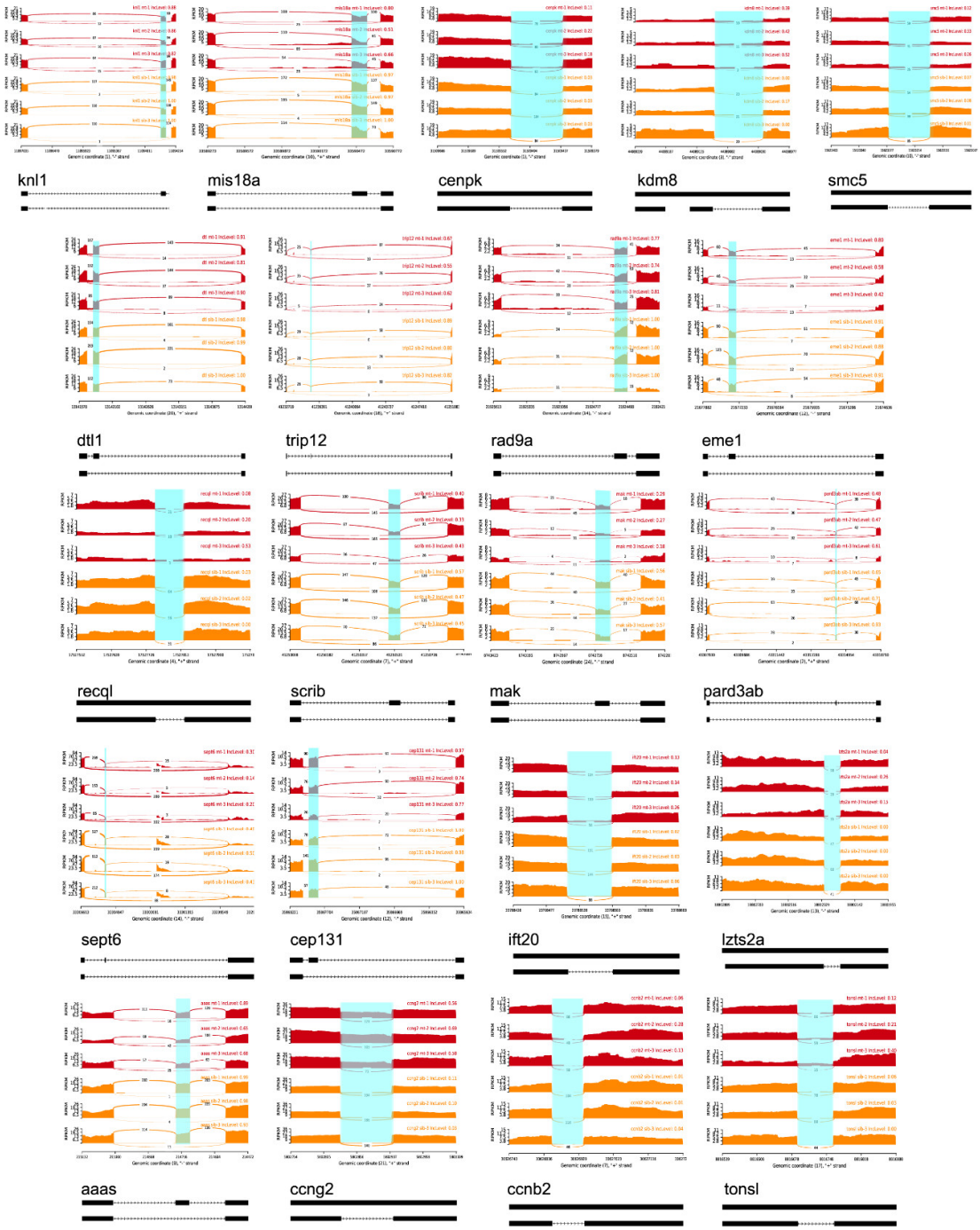

Fig. S7. Sashimiplot visualization of alternative splicing changes in selected genes in Fig 7. Junction reads and IncLevels were assessed by IGV to further confirm the presence of selected differential spliced genes in Fig 7 between wild-type sibling and *dhx38* mutants.

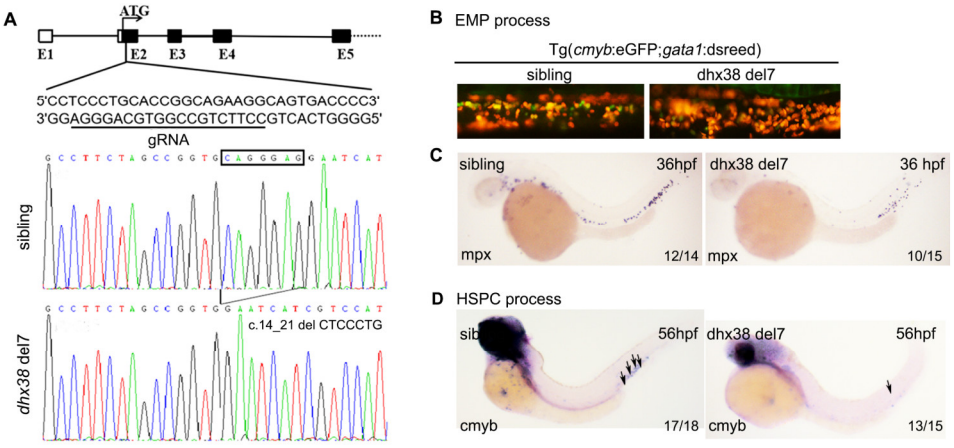

Fig S8. Enhanced EMP progenitor and impaired HSPC maintenance in *dhx38* del 7 mutants.

A A schematic diagram of the *dhx38* gRNA locus. DNA sequencing identified a 7 bp deletion of cDNA (c.14_21delCTCCCTG), which predicts a truncated protein (p.Ser5_ThrfsTer8). **B** In vivo imaging of EMPs and HSPCs in the PBI region of Tg(*cmyb*:eGFP;*gata1*:dsred) fish at 36 hpf. The number of EMPs and HSPCs in the *dhx38*$^{-/-}$ zebrafish is higher than that in wild-type siblings. **C** WISH results reflecting the expression of mature myelocytes (*mpx*) is decreased in the *dhx38* del7 mutant at 36 hpf. **D** The expression of the hematopoietic progenitor cells marker *cmyb* at 56 hpf in siblings and *dhx38* del7 mutants. The black arrows indicate the position of the *cmyb* gene expression.

Table S1. Significantly differentially expressed genes in the *dhx38* mutants.

Click here to download Table S1

Table S2. GO enrichment of significantly differentially expressed genes in Table S1.

Click here to download Table S2

Table S3. All significantly differentially alternatively spliced events in the *dhx38* mutants and the prediction of gene transcript swift after differential splicing.

Click here to download Table S3

Table S4. All significantly differentially spliced genes and GO enrichment of differentially spliced genes.

Click here to download Table S4

Table S5. All Primers used in this study, including those for semi-PCR, qRT-PCR, identification of dhx38 genotype primers, and WISH probes.

Click here to download Table S5

Table S6. Antibodies used in this study

Antibodies	Source	Cat#	RRID	Dilution
Anti-α-Tubulin	GeneTex	GTX76511	AB_378784	1:100 for IF
Anti-pH3	Affinity	AF3358	AB_2834773	1:200 for IF
Anti-GFP	Dai-an	2057	N.A.	1:200 for IF
Anti-mcherry	Affinity	T0090	AB_2843441	1:200 for IF
DAPI	Thermo Fisher Scientific	D1306	AB_2629482	1:1000 for IF
Goat anti-Rabbit IgG (H+L) Secondary Antibody, Alexa Fluor 594	Thermo Fisher Scientific	A-11012	AB_2534079	1:1000 for IF
Goat anti-Rabbit IgG (H+L) Secondary Antibody, Alexa Fluor 488	Thermo Fisher Scientific	A-31565	AB_2536178	1:1000 for IF
Goat anti-Mouse IgG (H+L) Secondary Antibody, Alexa Fluor 488	Thermo Fisher Scientific	A-11001	AB_2534069	1:1000 for IF
Goat anti-Mouse IgG (H+L) Secondary Antibody, Alexa Fluor 594	Thermo Fisher Scientific	A-11005	AB_2534073	1:1000 for IF
Goat anti-Rat IgG (H+L) Secondary Antibody, Alexa Fluor 647	Thermo Fisher Scientific	A-21247	AB_141778	1:1000 for IF
Anti-P53	GeneTex	GTX128135	AB_2864277	1:500 for WB
Anti-GAPDH	Dia-an	2058	N.A.	1:500 for WB
Goat anti-Rabbit IgG (H+L) Secondary Antibody, HRP	Thermo Fisher Scientific	31460	AB_228341	1:20000 for WB
Goat anti-Mouse IgG (H+L) Secondary Antibody, HRP	Thermo Fisher Scientific	31430	AB_228307	1:20000 for WB
Anti-DHX38	Proteintech	10098-2-AP	AB_2092294	1:1000 for WB
Phospho-Histone H2A.X (Ser139) Antibody	Cell Signaling Technology	2577	AB_2118010	1:1000 for WB
Anti-SMC5	Proteintech	14178-1-AP	AB_2192775	1:1000 for WB
Anti-CCNB2	Thermo Fisher Scientific	PA5-86965	AB_2803721	1:1000 for WB

Table S7. Sequences of siRNAs used in this study

siRNA	Sequence	
Negative control (Nc)	5’-3’	UUCUCCGAACGUGUCACGUTT
	3’-5’	ACGUGACACGUUCGGAGAATT
DHX38-Homo-641	5’-3’	GCGGGAACAUGGUGUCUAUTT
	3’-5’	AUAGACACCAUGUUCCCGCTT
DHX38-Homo-325	5’-3’	GCGAGCAGCAUGUCUUCAATT
	3’-5’	UUGAAGACAUGCUGCUCGCTT